

# We are IntechOpen, the world's leading publisher of Open Access books Built by scientists, for scientists

6,900

Open access books available

186,000

International authors and editors

200M

Downloads

Our authors are among the

154

Countries delivered to

TOP 1%

most cited scientists

12.2%

Contributors from top 500 universities



WEB OF SCIENCE™

Selection of our books indexed in the Book Citation Index  
in Web of Science™ Core Collection (BKCI)

Interested in publishing with us?  
Contact [book.department@intechopen.com](mailto:book.department@intechopen.com)

Numbers displayed above are based on latest data collected.  
For more information visit [www.intechopen.com](http://www.intechopen.com)



---

# Novel Measurement Methods for Thermoelectric Power Generator Materials and Devices

---

Patrick J. Taylor, Adam Wilson, Jay R. Maddux,  
Theodorian Borca-Tasciuc, Samuel P. Moran,  
Eduardo Castillo and Diana Borca-Tasciuc

Additional information is available at the end of the chapter

<http://dx.doi.org/10.5772/65443>

---

## Abstract

Thermoelectric measurements are notoriously challenging. In this work, we outline new thermoelectric characterization methods that are experimentally more straightforward and provide much higher accuracy, reducing error by at least a factor of 2. Specifically, three novel measurement methodologies for thermal conductivity are detailed: steady-state isothermal measurements, scanning hot probe, and lock-in transient Harman technique. These three new measurement methodologies are validated using experimental measurement results from standards, as well as candidate materials for thermoelectric power generation. We review thermal conductivity measurement results from new half-Heusler (ZrNiSn-based) materials, as well as commercial  $(\text{Bi,Sb})_2(\text{Te,Se})_3$  and mature PbTe samples. For devices, we show characterization of commercial  $(\text{Bi,Sb})_2(\text{Te,Se})_3$  modules, precommercial PbTe/TAGS modules, and new high accuracy numerical device simulation of Skutterudite devices. Measurements are validated by comparison to well-established standard reference materials, as well as evaluation of device performance, and comparison to theoretical prediction obtained using measurements of individual properties. The new measurement methodologies presented here provide a new, compelling, simple, and more accurate means of material characterization, providing better agreement with theory.

**Keywords:** thermal conductivity, Seebeck coefficient, electrical resistivity, ZT, device efficiency

---

## 1. Introduction

The efficiency with which a thermoelectric (TE) power generator can convert heat energy to electricity is determined, in part, by thermal conductivity,  $\kappa$ , of the materials used for fabricating TE devices. Experimental measurement of that property usually results in surprisingly

---

significant error,  $>\pm 10\%$  [1]. There are many causes of that error, and in this chapter, we provide new solutions which are experimentally faster, yield results which are more consistent with physical devices, and address several sources of experimental error, which may reduce uncertainty by a factor of 2 or more.

In this work, we describe several new, more accurate techniques to measure thermal conductivity,  $\kappa$ , of thermoelectric materials. The first is based on detailed control of the heat flows within a sample under steady-state conditions; the so-called *steady-state isothermal technique*. The second is nondestructive microscale analysis technique called *scanning hot-probe (or scanning thermal microscopy)*. And the third is *lock-in transient Harman* method, which is a comprehensive modification of transient Harman technique, employing a lock-in procedure and considers detailed contact effects. A new interesting follow-on is frequency-dependent Nyquist analysis, which presages a different perspective on the material analysis.

The truest test of the accuracy of measurement is comparison with fabricated devices. To support the validation of measurements of individual material properties, we outline a new device metrics, which allows comparison between theoretical and measured device efficiency. We outline a new *slope-efficiency method*, which can be used to determine informative index  $ZT_{\text{maximum}}$  of any device. The second method of device evaluation is a numerical device model called the *discretized heat balance model*, which considers a piecewise continuous collection of discrete layers within a device, where boundary heat flows have energy and current continuity relationships, and enable incredibly easy determination of device efficiency.

## 2. Novel measurements of thermal conductivity

### 2.1. Steady-state isothermal technique

This new measurement of  $\kappa$  leverages Peltier heat,  $\pm Q_{\text{IT}}$ , an electronically controlled internal heat source unique to thermoelectric materials. Peltier heat causes either heating ( $+Q_{\text{IT}}$ ) or cooling ( $-Q_{\text{IT}}$ ) at the junction between a thermoelectric material and a metal by passing the proper polarity of electric current,  $\pm I$ .

$Q_{\text{IT}}$  was first employed to roughly estimate  $\kappa$  by Putley [2]. In Putley's experiment, convective, parasitic, and nonsymmetric heat flows required correction factors larger than 20%. Harman dramatically improved upon Putley's demonstration by performing the measurements in vacuum, and by reducing other parasitic heat flows. Despite these improvements, error is still obtained, because parasitic heat flows are nonzero [3].

In these past studies, principal parasitic heat flows causing error include conduction along lead wires, conduction along thermocouples, Joule heating within lead wires, and radiation. The magnitudes of these parasitic heat flows can be as large as 30% of Peltier heat. Penn quantified the significance of parasitic heat flows in Harman's technique, and showed, that they induced error of more than 10% [4]. Bowley and Goldsmid [5], as well as Buist [6] reported, that parasitic heat flows cause error, usually larger than 20%.

The focus of the present work is description of a new, correctionless method to measure  $\kappa$  by balancing two independently controlled heat sources:  $Q_{IT}$  and a radiatively coupled input heat as per the Stefan-Boltzmann law,  $Q_{SB}$ . In this new method,  $Q_{IT}$  and  $Q_{SB}$  can be independently balanced. A finite temperature difference across the sample imposed by  $Q_{SB}$  can be cancelled and even inverted by application of  $Q_{IT}$ . When exactly cancelled, there is no temperature difference across the sample (i.e.,  $\Delta T = 0$ ) and a steady-state isothermal condition is obtained leaving the steady-state temperature of the sample exactly equal to that of the surroundings,  $T_e$ . Because there is no  $\Delta T$ , parasitic heat flows, such as those along lead-wires/thermocouples ( $Q_{wires}$ ) and radiative heat loss, ( $Q_{radiation-error}$ ), which would otherwise cause significant error [7], converge exactly to zero. Analysis of this technique using a Peltier cooler demonstrates error of less than  $\pm 1\%$ , an improvement of over an order of magnitude [8]. When considering thermoelectric power generators, other considerations must be taken into account to determine experimental uncertainty (such as view angle for radiative heat flows from the environment, material emissivity, etc.), which are more complicated and beyond the scope of the work presented here. However, as is demonstrated qualitatively here, experimental uncertainty is reduced using the steady-state isothermal technique by significantly more than a factor of 2.

Assume a sample having the temperature of one end anchored to the temperature of the environment,  $T_e$ , by a large heat-sink, and the opposite end,  $T_{top}$ , having small thermal mass and capable of temperature diversion by the application of  $Q_{SB}$ . Vacuum is used to obviate convective heat flow, and  $Q_{SB}$  is applied by small heater having approximately the same subtended area as that of the cross-sectional area ( $A$ ) of the sample, such that  $Q_{SB}$  is localized to the top and there is no direct line of sight along the length of the sample ( $\ell$ ). Thermocouples are attached to each end to determine the temperature difference across the sample, and electrical leads are used for passing  $\pm I$  to control  $Q_{IT}$ . **Figure 1** depicts this experimental setup.

When  $Q_{SB}$  is applied, the temperature of the heated contact will increase with respect to  $T_e$  and some magnitude of  $Q_{\kappa}$  will be conducted through the sample. At the heated contact, contributing heat flows include  $Q_{SB}$ ,  $Q_{\kappa}$ ,  $Q_{radiation-error}$ , and  $Q_{wires}$ . Radiation-error flow  $Q_{radiation-error}$  is governed by the emissivity ( $\epsilon$ ), Stefan-Boltzmann constant ( $\sigma$ ), sidewall temperature ( $T_{sidewall}$ ), and sidewall area ( $A_{sidewall}$ ) of the sample.  $Q_{wires}$  follows the usual Fourier's law description where, for simplicity, aspect ratio ( $A_{wires}/\ell_{wires}$ ) and thermal conductivity ( $\kappa_{wires}$ ) of all wires and thermocouples are combined into one lumped parasitic term. When electrical current flows through the sample,  $Q_{IT}$  is absorbed at the heated contact, where the first Kelvin relation gives  $Q_{IT} = (\alpha_{sum}IT)$  and  $\alpha_{sum}$  is the sum of Seebeck coefficients of the sample and the contact metal, and  $T$  is the temperature of the heated contact. An equal and opposite value of  $Q_{IT}$  is liberated at the contact between the sample and large heat-sink, but is too small to cause any measurable temperature change of the heat-sink, and is therefore negligible. Including  $Q_{IT}$  at the heated contact yields Eq. (1), which, under steady-state conditions sums to zero:

$$\sum Q = Q_{SB} - Q_{IT} - Q_{\kappa} - Q_{radiation-error} - Q_{wires} = 0. \quad (1)$$

To quantify the magnitude of  $Q_{\kappa}$ , a range of electrical currents can be passed, which enables  $Q_{IT}$  to absorb a corresponding range of  $Q_{SB}$  at the contact, so we get:

$$Q_{SB} = (\alpha_{\text{sum}}IT) + \left[ \kappa \left( \frac{A}{\ell} \right) \Delta T \right] + \varepsilon \sigma A_{\text{sidewall}} (T_{\text{sidewall}}^4 - T_e^4) + \left[ \kappa_{\text{wires}} \left( \frac{A_{\text{wires}}}{\ell_{\text{wires}}} \right) \Delta T \right]. \quad (2)$$

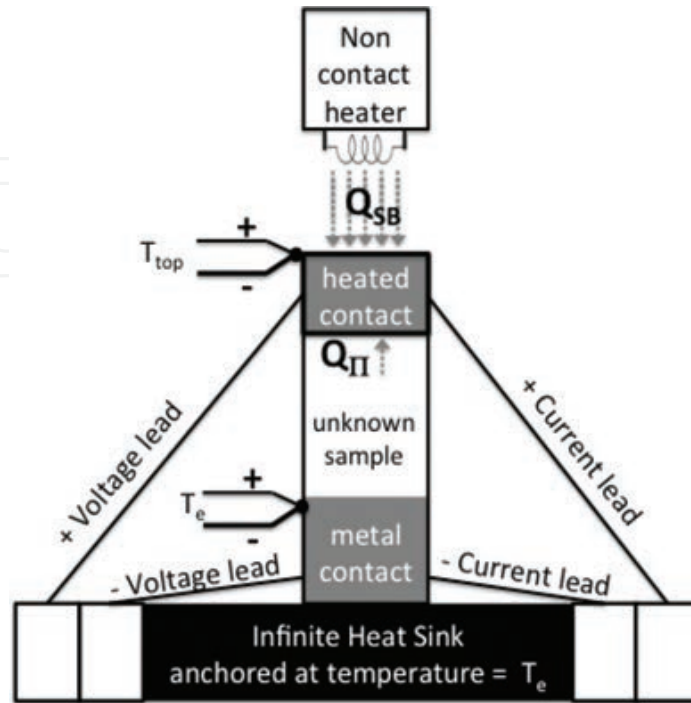


**Figure 1.** Experimental schematic representation of steady-state isothermal technique.

For progressively larger  $I$ ,  $Q_{II}$  absorbs increasingly more of  $Q_{SB}$  and temperature of the heated contact begins to converge to  $T_e$ , such that the overall  $\Delta T$  across the sample goes to zero. As  $\Delta T$  becomes smaller with increasing  $I$ , the only relevant heat flows are  $Q_{SB}$ ,  $Q_{II}$ , and  $Q_{\kappa}$  because  $Q_{\text{radiation-error}}$  and  $Q_{\text{wires}}$  are only statistically significant [7] for larger  $\Delta T$ , say  $>10$  K, and all parasitic heat flows converge to zero. Therefore, under these conditions at any given  $I$ ,  $\Delta T$  across the sample is required to satisfy Eq. (3):

$$Q_{SB} = (\alpha_{\text{sum}}IT) + \left[ \kappa \left( \frac{A}{\ell} \right) \Delta T \right]. \quad (3)$$

From the requirement imposed by Eq. (3), a new method for measuring  $\kappa$  is obtained. Eq. (3) is solved to show the dependence of  $\Delta T$  on electrical current. By taking the derivative of Eq. (3), prior knowledge of  $Q_{SB}$  is not required, because it is a constant, and the analysis yields the following:

$$\frac{\partial \Delta T}{\partial I} = - \left[ \frac{\alpha_{\text{sum}} T}{\kappa \left( \frac{A}{\ell} \right)} \right]. \quad (4)$$

To determine  $\kappa$ , Eq. (4) is solved using the slope at  $\Delta T = 0$  of steady-state  $\Delta T$  as function of  $I$  and that slope is combined with  $\alpha_{\text{sum}}$ , as well as geometrical aspect ratio ( $A/\ell$ ) of the sample [8]. **Figure 2** shows dependence of the temperature difference between ends of the thermoelement sample on value of passing current (left panel) and real picture measurement configuration (right panel).

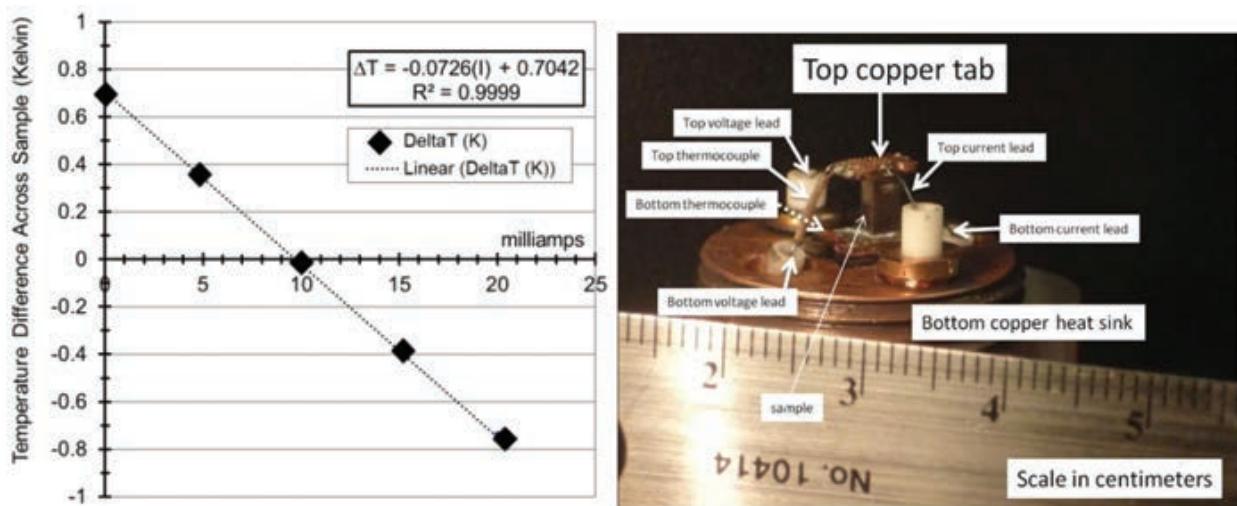


**Figure 2.** (Left) Linear  $\Delta T$  decrease across sample by application of milliamps of current (I) for Peltier cooling and (right) picture showing a fully connected sample.

### 2.1.1. Thermal conductivity of n-type half-Heusler

Thermal conductivity of a half-Heusler alloy (**Figure 3**) was collected (triangles) and is presented with respect to previously published data (squares, circles, and diamonds) measured by the laser-flash thermal diffusivity technique and reported by researchers from GMZ corporation [9]. Because of the speed, ease, and simplicity of the new technique presented, there is opportunity for significantly more collected data. One data point can be collected in seconds. However, as can be seen in **Figure 3**, it is consistent to within experimental error and falls within the bounds of the published laser-flash data.

### 2.1.2. Thermal conductivity of PbTe

One category of high performance thermoelectric materials is near-degenerate semiconductors. Such materials do not directly obey the Wiedemann-Franz relationship between electrical resistivity and thermal conductivity, due to the significant contribution of lattice thermal conduction to the total thermal conductivity. However, utilizing a modified Wiedemann-Franz relationship to find the thermal conductivity due to electron flow allows direct, real-time deconvolution of lattice thermal conductivity ( $\kappa_{\text{lattice}}$ ) from electronic contribution ( $\kappa_{\text{electronic}}$ ). For charge carriers concentrations near degeneracy, and random scattering of charge carriers, Rosi et al. [10] describe how  $\kappa_{\text{electronic}}$  can be determined using electrical resistivity,  $\rho$ , by:

$$\kappa_{\text{electronic}} = \left(\frac{\pi^2}{3}\right) \left(\frac{k_B}{q}\right)^2 \left(\frac{T}{\rho}\right). \quad (5)$$

If thermal conductivity and electrical resistivity are measured, then  $\kappa_{\text{lattice}}$  can be determined by  $\kappa_{\text{lattice}} = [\kappa - \kappa_{\text{electronic}}]$ .

**Figure 4** shows temperature dependences of PbTe thermal conductivity (including measured data) and deconvolution of electronic and lattice contributions to total thermal conductivity.

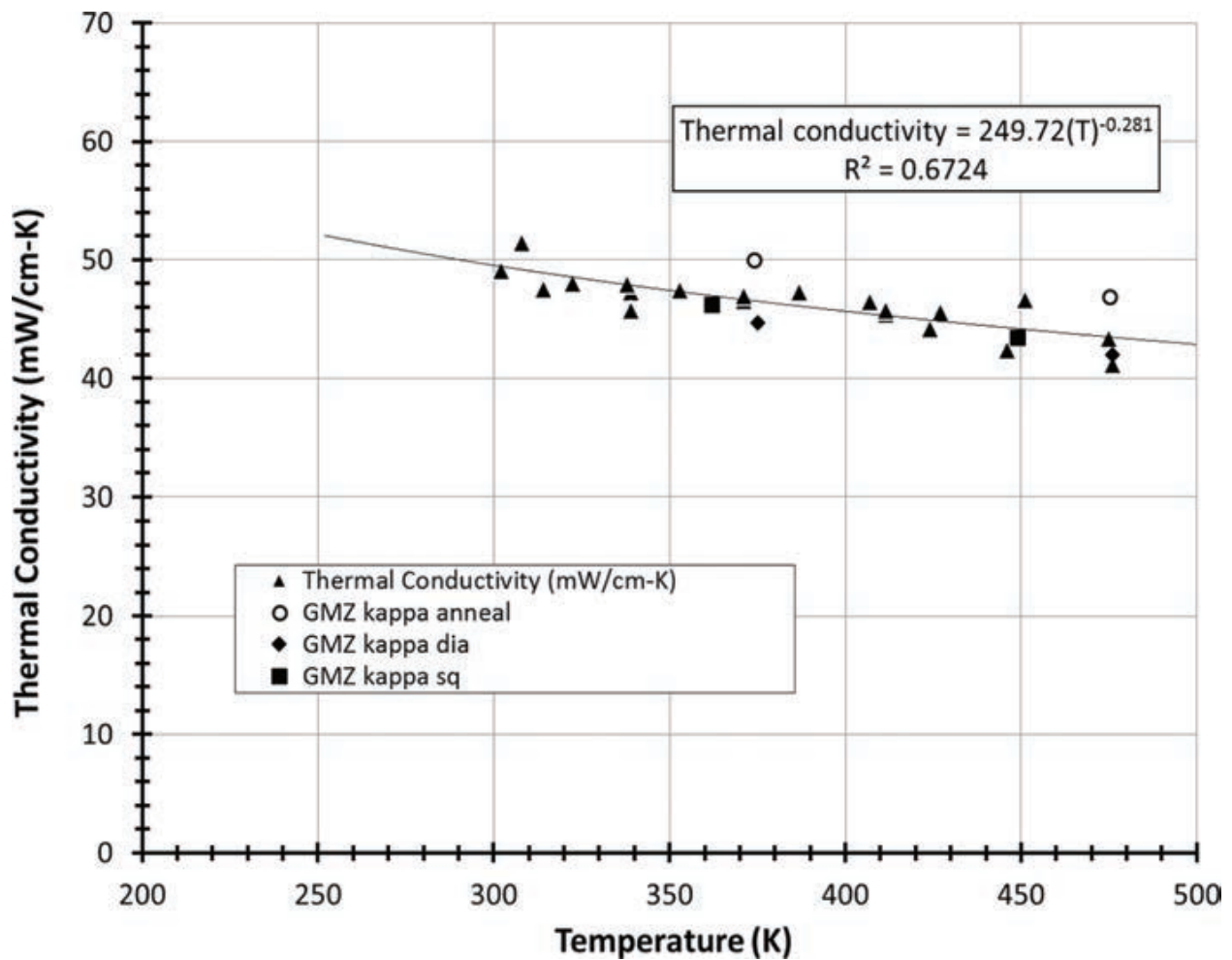


Figure 3. Thermal conductivity of n-type half-Heusler measured by steady-state isothermal technique as compared to published data [9].

## 2.2. Scanning hot probe

The scanning hot probe technique provides measurement of local thermal conductivity and Seebeck coefficient of a sample by measuring average probe temperature when probe tip and sample are in “thermal contact”, i.e., when probe tip is in physical contact with the sample or is at known distance near enough to the sample to induce measurable heat exchange between probe and sample. Average probe temperature is also measured far from the sample, to account for the amount of heat lost to the surroundings and through the probe contacts. Difference in average probe temperature between these two cases is due to the heat transferred to the sample, which may be quantified through the following analytical derivation. **Figure 5** depicts the thermal exchange between probe, sample, and surroundings, as well as the series thermal resistance network between probe and sample.

For steady-state probe heating using DC current, (or AC current at low frequency, when the heat capacity effects are negligible, and temperature rise amplitude is frequency independent and equivalent to DC temperature rise to good approximation) the governing equation describing amplitude of the temperature profile of the probe shown in **Figure 5** is given by [12]:

$$\frac{d^2 T^*}{dx^2} - \left( \frac{2h_{\text{eff}}}{\kappa_P r} - \frac{I^2 \rho_0 \text{TCR}}{\kappa_P \pi^2 r^4} \right) T^* + \frac{I^2 \rho_0}{\kappa_P \pi^2 r^4} = 0, \quad (6)$$

where  $T^* = T(x) - T_0$ ,  $h_{\text{eff}} = h + 4\epsilon\sigma T_0^3$  (here,  $h$  is the convective heat transfer coefficient,  $\epsilon$  is the probe's emissivity,  $T_0^3$  is an approximation for the exact  $(T^4 - T_0^4)$  term and  $\sigma$  is Stefan-Boltzmann constant.  $\rho_0$  and  $\kappa_P$  are the probe's electrical resistivity and thermal conductivity, respectively, TCR is the probe's temperature coefficient of resistance,  $I$  is root-mean-square electrical current passed through the probe, and  $r$  is the radius of the probe. Contribution from radiation is negligible for  $\Delta T < 100$  K [13].

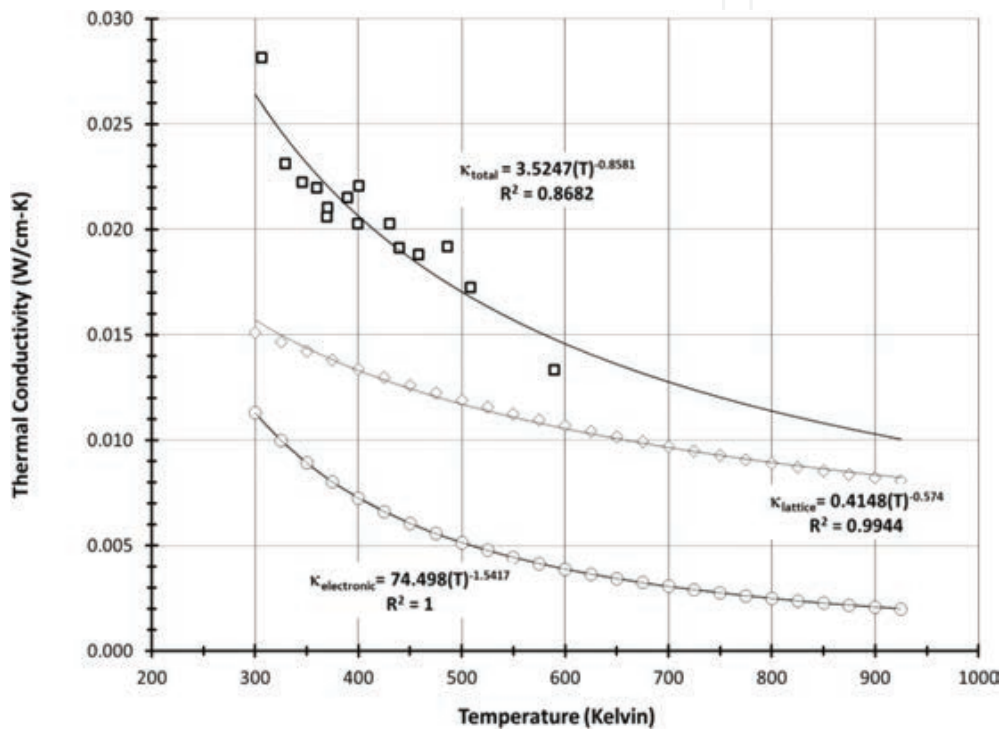


**Figure 4.** Measurement of thermal conductivity of PbTe, and deconvolution of electronic and lattice contributions to the total thermal conductivity.

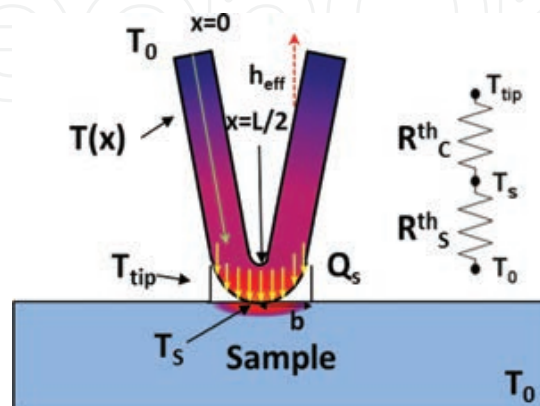


**Figure 5.** Diagram showing thermal phenomenology around probe tip. Reproduced from [11] with permission from The Royal Society of Chemistry.

To obtain an analytical solution to the second order differential equation, two boundary conditions are employed. The first assumption is that the ends of the probe are at ambient temperature (i.e.,  $T(0) = T_0$ ). The second assumption is that the tip region of the probe of length  $2b$  is of uniform temperature, and by energy balance at the probe tip region, we get:

$$-\kappa_P A \frac{dT^*}{dx} \Big|_{x=L/2-b} + I^2 \rho_0 (1 + TCR \times T^* \Big|_{x=L/2-b}) \frac{b}{A} = \frac{Q_s}{2}, \quad (7)$$

where the left-hand side is heat conduction and Joule heating of the probe,  $A = \pi r^2$  is the probe's cross-sectional area, and  $L$  is the length of the probe, and where the right-hand side is heat transfer through one leg of the probe (thus half the total heat transfer to the sample, by symmetry). Finally, heat transfer rate between probe and sample,  $Q_s$ , is:

$$Q_s = \frac{\Delta T_{\text{tip}}}{R_C^{\text{th}} + R_S^{\text{th}}} = \frac{\Delta T_S}{R_S^{\text{th}}}, \quad (8)$$

where  $\Delta T_{\text{tip}} = T_{\text{tip}} - T_0$  and  $\Delta T_S = T_S - T_0$  are temperature of the probe and sample, respectively, at the tip region, and  $R_S^{\text{th}}$  is samples thermal resistance. Solving Eq. (6) to obtain temperature profile along the probe for a given value of  $Q_s$  yields the following expression:

$$\Delta T_P(x) = C_1 e^{\lambda x} - C_2 e^{-\lambda x} + \frac{\Gamma}{\lambda^2}, \quad (9)$$

where  $\lambda = \frac{I^2 \rho_0}{\kappa_P \pi^2 r^4}$ ,  $\Gamma = \frac{2h_{\text{eff}}}{\kappa_P r} - \frac{I^2 \rho_0 TCR}{\kappa_P \pi^2 r^4}$ , and constants  $C_1$  and  $C_2$  are easily obtained by applying boundary condition  $T(0) = T_0$ .

If the sample is bulk, or has bulk-like thickness, thermal conductivity is found from  $R_S^{\text{th}}$  by employing semiinfinite medium assumption and 2D bulk sample assumption [14]:

$$R_S^{\text{th}} = \frac{1}{4\kappa_{\text{sample}} b}. \quad (10)$$

If the sample is a thin film of thickness  $l$  on substrate, and is thin enough, that there is negligible heat spreading in the in-plane directions of the sample, then thermal conductivity is found by solving the expression for the series thermal resistance across substrate and film, with 1D heat transfer across the thickness of the film [14]:

$$R_S^{\text{th}} = \frac{1}{4\kappa_{\text{substrate}} b} + \frac{l}{\pi \kappa_{\text{film}} b^2}. \quad (11)$$

When heat transfer may be multidimensional and anisotropic, models developed by Son et al. [15] for laser heating may be used to predict thermal resistance of the sample, based on the respective values of thermal conductivity for the film and substrate.

Data collected from scanning hot thermoelectric probe experiment are probe voltage, voltage across a reference resistor, Seebeck voltage, and photodetector voltage for position sensing. The value of current passing through the system is obtained by dividing voltage across the

reference resistor by known electrical resistance of that resistor. Probe resistance is then found by dividing probe voltage by that value of current. Often, instead of single reference resistor, Wheatstone bridge is utilized. **Figure 6** depicts the difference in circuit between measurement taken (a) with and (b) without Wheatstone bridge.

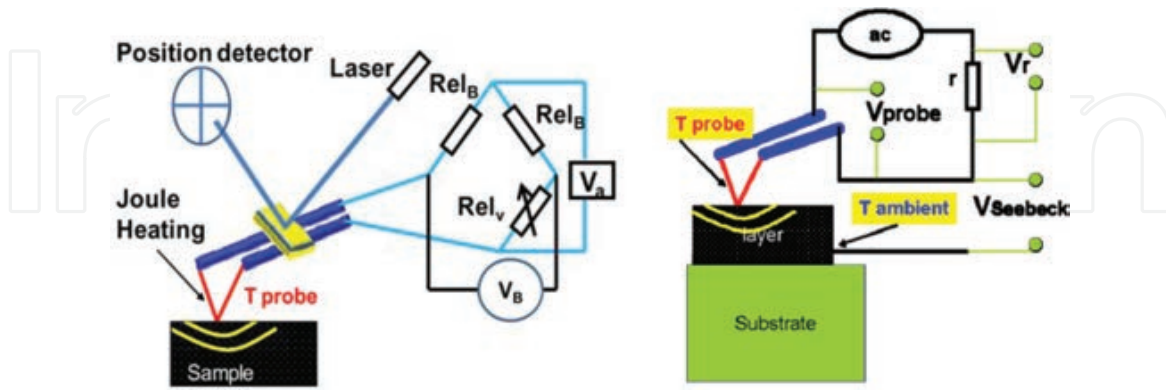


**Figure 6.** Schematic scanning thermal microscopy circuits (left) with Wheatstone bridge and (right) with a reference resistor.

In DC mode, with resistor wired in series with the probe, measured probe voltage,  $V_P$ , may be expressed in terms of voltage across reference resistor ( $V_r$ ) as:

$$V_P = R_P I = \frac{R_P V_r}{R_r}, \quad (12)$$

where  $I$  is DC current passing through the circuit,  $R_P$  is electrical resistance of the probe, and  $R_r$  is known electrical resistance of reference resistor. Probe's electrical resistance is proportional to temperature rise above ambient, when the probe undergoes Joule heating. It may be expressed as:

$$R_P = \Delta T_P (R_0 \text{TCR}) + R_0 + R_c, \quad (13)$$

where  $\Delta T_P$  is average probe temperature rise,  $R_0$  is nominal probe electrical resistance at 19.9°C, (not including electrical contacts to the circuit), when the probe is not being heated,  $R_c$  is electrical resistance arise from contacts and circuit's wiring, and TCR is probe's temperature coefficient of resistance, in terms of 1/°C.

Defining average probe thermal resistance as average probe temperature rise divided by Joule heating power, we can write average probe thermal resistance as:

$$R_P^{\text{th}} = \frac{\Delta T_P}{I^2 R_0 (1 + (\text{TCR}) \Delta T_P)}. \quad (14)$$

Eq. (14) allows determination of  $R_P^{\text{th}}$  by the slope of probe temperature rise with power applied, reducing the overall experimental uncertainty compared with a single value of temperature at a given power. If the circuit uses Wheatstone bridge, equations differ only by the method of finding electrical resistance of the probe. In this case,  $R_P$  reduces to:

$$R_P = R_0 + \frac{V_B (R_B + R_0)^2}{V_A R_B} + R_c, \quad (15)$$

where  $V_B$  and  $V_A$  are voltages across bridge side and probe side, respectively.  $R_B$  is the total resistance of bridge side of the circuit, and  $R_0$  is no heating resistance of the probe side of the bridge. With the probe resistance obtained, remaining equations are left unchanged. When AC current of amplitude  $I_0$  is passed through the circuit, then measured probe resistance can be expressed as:

$$R_P = \underbrace{R_0 \left( 1 + (TCR) \Delta T_{P,DC} \right)}_{DC \text{ Component}} + \underbrace{R_0 (TCR) \Delta T_{P,2\omega} \cos(2\omega t + \phi)}_{AC \text{ Component}}. \quad (16)$$

The probe tip voltage is expressed as:

$$V = I_0 R_P \left( 1 + (TCR) \Delta T_{P,DC} \right) \cos(\omega t) + \frac{I_0 R_P (TCR) \Delta T_{P,2\omega}}{2} [\cos(3\omega t + \phi) + \cos(\omega t + \phi)]. \quad (17)$$

Thus, temperature amplitude is determined to be:

$$\Delta T_{ave} = \frac{2V_{3\omega}}{(TCR)V_{1\omega}}. \quad (18)$$

To obtain sample thermal conductivity, the probe must be calibrated. Quantities in Eqs. (6)–(11), which are not determined directly from experimental measurement are:  $h_{eff}$ , TCR,  $k_P$ ,  $A$ ,  $L$ ,  $\rho_0$ ,  $b$ , and  $R_C^{th}$ . To be fully calibrated, these quantities must be known. The probe manufacturer specifies values for TCR,  $k_P$  and  $\rho_0$ , and these values are used in this work. Values  $A$  and  $L$  may be found by determining probe's geometry (typically from SEM or microscope images, but may also be determined by measuring  $R_P^{th}$  in a vacuum and in air).  $h_{eff}$  is determined by measuring  $R_P^{th}$  far from contact, and matching the value predicted by the analytical model by adjusting  $h_{eff}$  and integrating Eq. (9) from  $x = 0$  to  $L$  and dividing by  $L$ , with  $Q_s = 0$  to obtain the average probe temperature when no heat is transferred to the sample. Finally, probe-to-sample thermal exchange parameters,  $b$  and  $R_C^{th}$ , must be determined. Typically, these values have been assumed to be sample-independent for given probe-to-sample contact force or probe-to-sample distance. As such, calibration strategies utilize measurements on two samples. However, these parameters are now shown to change with sample thermal conductivity. **Figure 7** demonstrates change in  $b$  and  $R_C^{th}$  with sample thermal conductivity. Alternatively, if the sample is electrically grounded and probe tip is capable of making good electrical contact with the sample, then sample with known thermal conductivity and Seebeck coefficient may be used to determine both  $b$  and  $R_C^{th}$  simultaneously. **Figure 7** demonstrates this calibration strategy, together with the typical "intersection method" using two or more samples. Care must be taken to calibrate in the correct range of thermal conductivity, as samples with thermal conductivity of higher than 1.1 W/mK yield a different pair of  $b$  and  $R_C^{th}$  values compared with samples with thermal conductivity of 1.1 W/mK and lower. **Table 1** presents the results of measurements taken with properly calibrated Wollaston probe tips, showing good agreement with independent measurements.

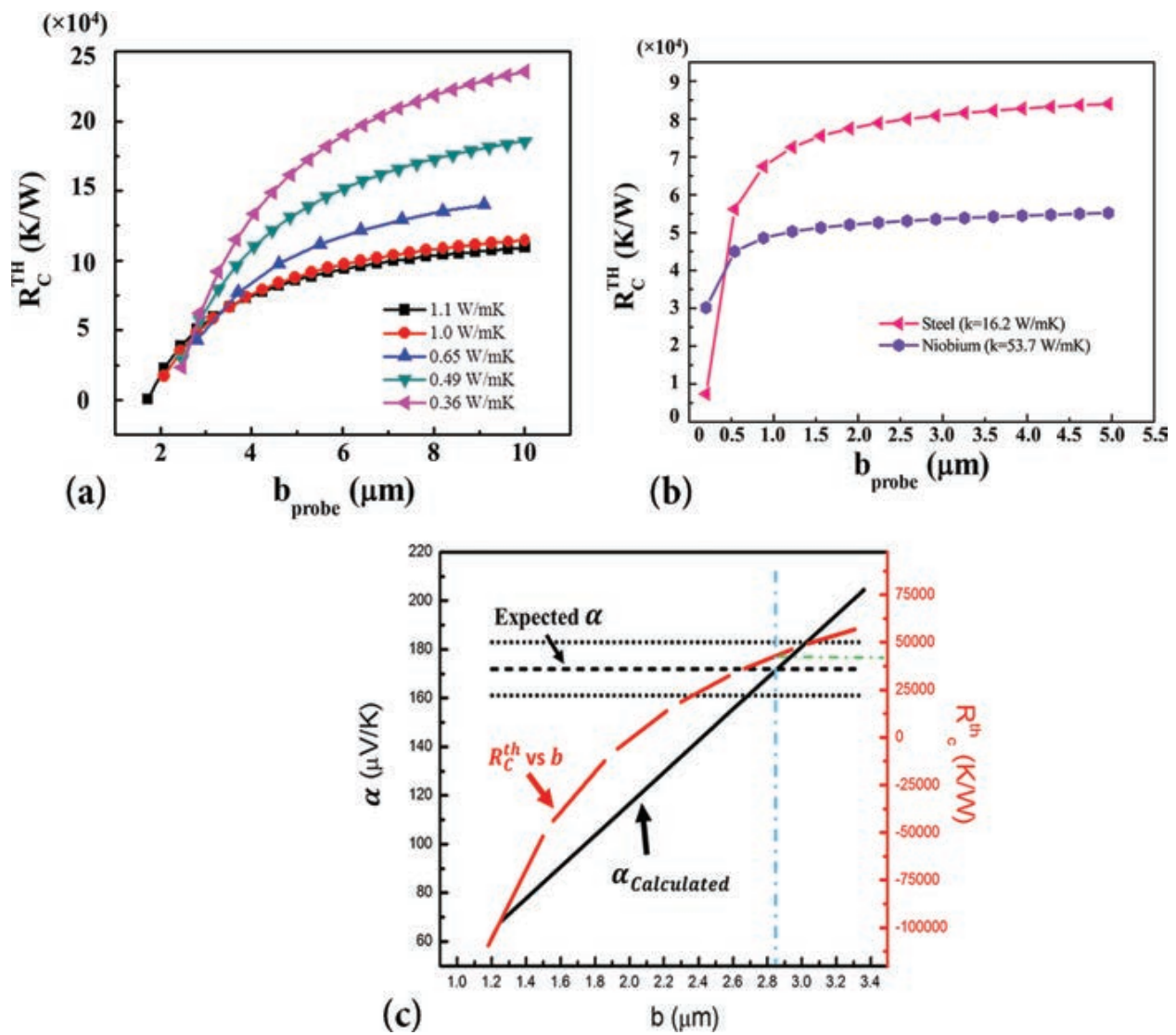


**Figure 7.** Empirical probe calibration strategies for determining  $b$  and  $R_C^{th}$  using (top) intersections of curves taken from samples with known  $\kappa$  for (left) low thermal conductivity and (right) high thermal conductivity and (bottom) determining  $b$  and  $R_C^{th}$  using a single sample with known  $\kappa$  and  $\alpha$ . Adapted from [11] with permission from The Royal Society of Chemistry.

### 2.3. Transient and lock-in Harman techniques to decouple material ZT and thermoelectric properties

Finally, a new method of measuring material thermal conductivity by simultaneously measuring thermoelectric figure of merit ( $ZT$ ), electrical resistivity ( $\rho$ ), and Seebeck coefficient ( $\alpha$ ) is proposed.  $ZT$  is dimensionless measure of the efficiency of material at converting thermal into electrical energy, or vice versa, at a given temperature,  $T$ , and may be expressed as:

$$ZT = \alpha^2 T / \rho \kappa. \quad (19)$$

Thus, thermal conductivity is obtained if the other terms in Eq. (19) are known. This new method also allows for measuring intrinsic  $ZT$  with reduced experimental error by accounting for losses through nonideal contacts and geometry.

Sample	$l$	$b$	$R_p^{th}$	$R_C^{th}$	$R_S^{th}$	$\kappa_{film}$ , this work // $\kappa_{film}$ , expected
SiGe film on glass substrate	1.8 $\mu\text{m}$	2.8 $\pm$ 0.3 $\mu\text{m}$	14.948 $\pm$ 54 K/W	44.927 $\pm$ 7820 K/W	76.134 $\pm$ 9494 K/W	1.22 $\pm$ 0.21 W/K·m // 1.23 $\pm$ 0.12 W/K·m [16]
Fe-doped PCDTBT (1:1 doping concentration)	3.0 $\mu\text{m}$	2.8 $\pm$ 0.3 $\mu\text{m}$	15.220 $\pm$ 155 K/W	44.927 $\pm$ 7820 K/W	87.022 $\pm$ 14.631 K/W	1.03 $\pm$ 0.15 W/K·m [17]
PCDTBT (non-doped)	3.0 $\mu\text{m}$	2.8 $\pm$ 0.3 $\mu\text{m}$	17.866 $\pm$ 204 K/W	44.927 $\pm$ 7820 K/W	358.859 $\pm$ 66.204 K/W	0.25 $\pm$ 0.04 W/K·m // 0.20 $\pm$ 0.02 W/K·m [17]
Tellurium Film	2.74 $\mu\text{m}$	2.8 $\pm$ 0.3 $\mu\text{m}$	15.749 $\pm$ 75.5 K/W	44.927 $\pm$ 7820 K/W	112.476 $\pm$ 6.480 K/W	0.79 $\pm$ 0.04 W/K·m // 0.78 $\pm$ 0.08 W/K·m [18]
Au film on silicon substrate	150 nm	428 $\pm$ 24 nm	11.624 $\pm$ 157 K/W	40.191 $\pm$ 1532 K/W	5505 $\pm$ 253 K/W	104.2 $\pm$ 67.4W/K·m //110 $\pm$ 2 W/ K·m [19]
PEDOT <sup>CAL</sup>	Bulk	2.8 $\pm$ 0.3 $\mu\text{m}$	17.429 $\pm$ 217 K/W	44.927 $\pm$ 7820 K/W	241.732 $\pm$ 37.672 K/W	0.37 $\pm$ 0.05 W/K·m // 0.36 W/K·m
PANI-5 % GNP <sup>CAL</sup>	Bulk	2.8 $\pm$ 0.3 $\mu\text{m}$	17.018 $\pm$ 115 K/W	44.927 $\pm$ 7820 K/W	188.595 $\pm$ 27.836 K/W	0.47 $\pm$ 0.06 W/K·m // 0.49 W/K·m [20]
PANI-7 % GNP <sup>CAL</sup>	Bulk	2.8 $\pm$ 0.3 $\mu\text{m}$	16.314 $\pm$ 118 K/W	44.927 $\pm$ 7820 K/W	131.760 $\pm$ 25.913 K/W	0.68 $\pm$ 0.08 W/K·m //0.65 W/ K·m [20]
p-typeBi <sub>2</sub> Te <sub>3</sub> <sup>CAL</sup>	Bulk	2.8 $\pm$ 0.3 $\mu\text{m}$	15.700 $\pm$ 145 K/W	44.927 $\pm$ 7820 K/W	92.113 $\pm$ 11.911 K/W	0.97 $\pm$ 0.11 W/K·m // 1.0 W/K·m
Borosilicate Glass <sup>CAL</sup>	Bulk	2.8 $\pm$ 0.3 $\mu\text{m}$	15.516 $\pm$ 134 K/W	44.927 $\pm$ 7820 K/W	82.313 $\pm$ 9787 K/W	1.08 $\pm$ 0.11 W/K·m // 1.1 W/K·m
AISI 304 Steel <sup>CAL</sup>	Bulk	428 $\pm$ 24 nm	13.811 $\pm$ 119 K/W	40.191 $\pm$ 1532 K/W	37.511 $\pm$ 3511 K/W	15.6 $\pm$ 2.2 W/K·m // 16.2 W/K·m
Goodfellow®99.9 % pure Niobium <sup>CAL</sup>	Bulk	428 $\pm$ 24 nm	12.194 $\pm$ 140 K/W	40.191 $\pm$ 1532 K/W	10.632 $\pm$ 2329 K/W	54.9 $\pm$ 8.9 W/K·m // 53.7 W/K·m

**Table 1.** Tabular results for a range of materials [16–20]. Reproduced from [11] with permission from The Royal Society of Chemistry.

Conventional application of Harman method uses four probes—two to pass current, and two to measure the voltage response of the sample. Harman demonstrated that, while electrical response of the sample was nearly instantaneous, voltage generated by Seebeck effect, which is thermally driven, is much slower. By taking advantage of this fact, thermal signal could be determined from voltage response of the sample to a sudden change in voltage over time, or response to an AC current passed, locking into thermally driven signal. It was shown, by letting  $\alpha = V_\alpha/\Delta T$ ,  $\kappa = -\Delta TA/(\alpha TI)$ , and  $\rho = V_\rho A/(LI)$ , that ZT could be reduced to the ratio of resistive voltage to Seebeck voltage (*i.e.*,  $ZT = V_S/V_Q$ ). This assumes ideal contacts (negligible thermal and electrical losses through the contact leads) and that temperature rise is due only to Peltier heating, neglecting effects of Joule heating. However, these effects are often difficult to mitigate, and may be accounted for by appropriate modeling (see **Figure 8**).

From resistive voltage, one may be able to determine electrical resistivity of the material; however, Seebeck coefficient and thermal conductivity remain coupled in equation for ZT. To decouple them, Seebeck coefficient may be simultaneously determined by adding a pair of thermocouple wires at the top and bottom surfaces of the sample as per **Figure 9**. If we label electric potential in each corner of the sample  $E_1 - E_4$ , respectively, using Ivory technique [17], we may find Seebeck coefficient from taking voltage measurements across the sample. If voltage is measured at opposite corners, then voltage values measured are  $E_{13}$  and  $E_{24}$ . Value  $\alpha$  is determined from expression below, where  $m$  is the slope of  $E_{13}$  vs  $E_{24}$ :

$$\alpha_{\text{sample}} = \lim_{E_{13} \rightarrow E_{24}} \frac{1}{1-m} \alpha_{ba} + \alpha_b. \quad (20)$$

This technique for measuring Seebeck coefficient reduces the required number of voltage measurements to determine  $\alpha$  from three to two and mitigates mismatch in thermocouples, since DC offsets are removed by using a slope. It also allows for AC measurements of the total voltage, and determination of ZT from Nyquist diagrams.

### 2.3.1. Transient Harman technique—analytical model

Several experimental setups used by the research community for thermoelectric characterization of thin films employ clean room microfabrication techniques to pattern a metallic electrode on top of the sample, while others use bonded wires or micromanipulated probes to make electrical contact with the top surface of the film sample [3, 21–24]. Configuration modeled in this work is similar to these situations, as shown in **Figure 8**. Thermoelectric film (3) with cross-sectional area,  $A_3$ , is deposited on substrate; metallic electrode (2) covers the top film's surface; and electrically conductive probe wire (1) of diameter,  $d_1$ , is brought in contact with the top surface of the sample. Substrate electrode (4) situated at the interface between thermoelectric film and substrate is used to close the loop and pass current into the film. The substrate electrode is assumed to have negligible electrical and thermal resistance. Its contribution to thermoelectric transport is therefore neglected, with exception of Peltier effect. Substrate electrode temperature is assumed to be the same as the top surface of the substrate ( $T_b$ ). Electrical and thermal contact resistances expressed as specific values  $R_{C\_i-j}$  and  $R_{th\_i-j}$  are assumed at interfaces between adjacent layers indexed by  $i$  and  $j$ , with ( $j = i + 1$ ). Classical thermoelectric transport model, which neglects electron-phonon nonequilibrium effects, is

developed by assuming, that the thickness of thermoelectric film is much larger than phonon-electron thermalization length [25]. Under these conditions, thermoelectric transport in the probe, electrode, and sample is considered one-dimensional. In each layer  $i$ ,  $x$  is the spatial coordinate;  $h$ ,  $\kappa$ , and  $\rho$  are convection heat transfer coefficient, thermal conductivity and electrical resistivity, respectively;  $P$  is perimeter,  $T$  is absolute temperature,  $\alpha$  is Seebeck coefficient,  $A_3$  is area perpendicular to thermoelectric transport direction, and  $J$  is current density.

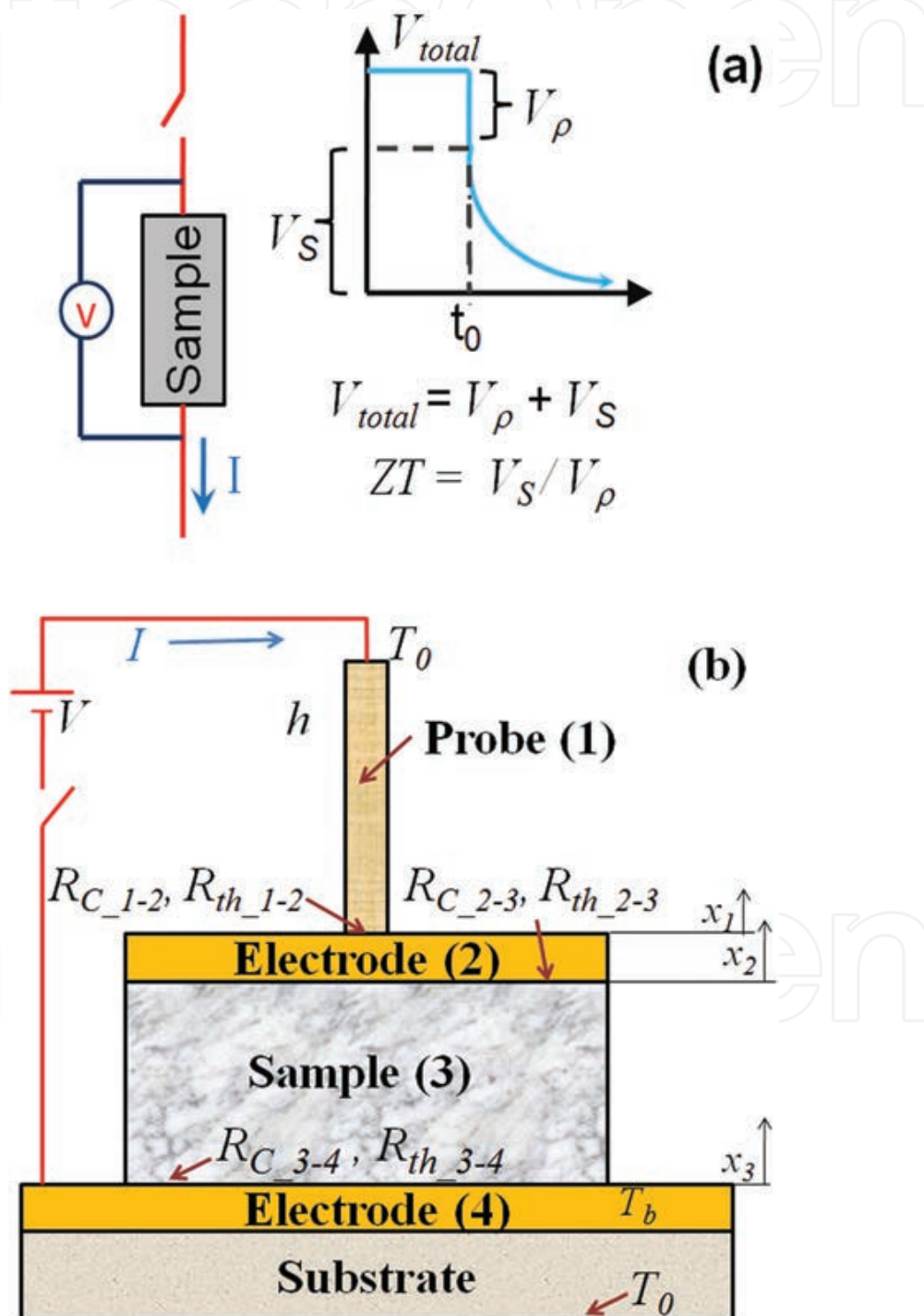


**Figure 8.** Schematic representation of lock-in Harman technique, under assumptions of (top) ideal contacts and (bottom) considering nonnegligible thermal and electrical resistances arise from contacts. Reprinted from [21] with the permission of AIP Publishing.

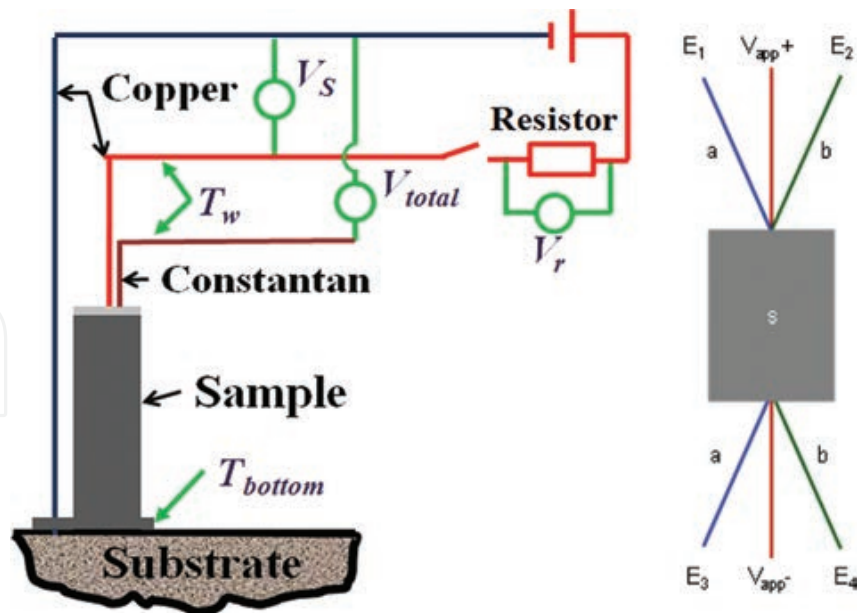


**Figure 9.** Schematic representation of sample measurement, including thermocouple contacts (ivory technique). (Left) sectional view (reprinted from [21] with the permission of AIP Publishing) and (right) view of sample from above.

Eq. (21) represents steady state energy balance in layers 1–3; the first term on the left side represents heat conduction, the second represents lateral convection and the third represents Joule heating. Thermal radiation and temperature dependence of thermoelectric properties have been neglected as small temperature differences are assumed to occur during the experiments.

$$\frac{d^2 T_i}{dx_i^2} - \frac{h_i P_i}{\kappa_i A_i} (T_i - T_0) + \frac{J_i^2 \rho_i}{\kappa_i} = 0; \quad i = 1, 2, 3. \quad (21)$$

General solution of Eq. (21) for temperature profile in the layer  $i$  is of the form,

$$T_i(x_i) = T_0 + c_{1,i} e^{\sqrt{\frac{h_i P_i}{\kappa_i A_i}} x_i} + c_{2,i} e^{-\sqrt{\frac{h_i P_i}{\kappa_i A_i}} x_i} + \frac{J_i^2 \rho_i A_i}{\kappa_i h_i}; \quad i = 1-3. \quad (22)$$

Integration constants  $c_{1,i}$  and  $c_{2,i}$  are determined using six boundary conditions. First, the temperature at free end of the probe of length  $l_1$  is assumed to be ambient temperature as stated by:

$$T_1 = T_0; x_1 = l_1. \quad (23)$$

Second, the temperature of the end of the probe in contact with the surface is assumed to be constant temperature (see expression in the ensuing discussion, Eq. (31)).

The third boundary condition considers energy conservation at the interface between the film and the substrate:

$$-\kappa_3 A_3 \frac{dT_3}{dx_3} \Big|_{x_3=0} + J_3 \alpha_3 A_3 T_3 \Big|_{x_3=0} = \frac{T_b - T_3 \Big|_{x_3=0}}{R_{th_{3-4}} / A_3} + \frac{1}{2} J_4^2 A_4 R_{C_{3-4}} = \frac{T_0 - T_b}{\Theta_{subst}} + J_4^2 A_4 R_{C_{3-4}} + J_4 \alpha_4 A_4 T_b. \quad (24)$$

In Eq. (24), the left side represents heat transfer rate out of the interface. It includes heat conduction and Peltier terms in layer 3, respectively. The middle section of Eq. (24) represents

one way to express heat transfer rate entering the interface. It is written as the sum of heat conduction across the interface thermal contact resistance and contact Joule heating term deposited at the interface in layer 3. It is assumed, that the total contact Joule heating is split equally on both sides of the interface. The right side of Eq. (24) represents the second way to express heat transfer rate entering the interface and includes: (1) substrate heat conduction transfer rate written as the temperature difference across the substrate divided by substrate's thermal conduction resistance; (2) total Joule heating due to electrical contact resistance; and (3) Peltier contribution due to electric current flowing through the substrate electrode. It is assumed, that the bottom surface of the substrate is at ambient temperature. Thermal conduction resistance of the substrate,  $\Theta_{\text{substr}}$  can be determined by conduction shape factor. For instance, for sample of diameter  $d_3$  on semiinfinite substrate with thermal conductivity  $\kappa_3$  shape factor is  $0.5 \kappa_3^{-1} d_3^{-1}$ .

Similar to Eq. (23), the fourth boundary condition is energy balance at the interface between probe and electrode:

$$\begin{aligned} -\kappa_1 A_1 \frac{dT_1}{dx_1} \Big|_{x_1=0} + J_1 \alpha_1 A_1 T_1 \Big|_{x_1=0} + h_2 (A_2 - A_1) (T_2 \Big|_{x_2=l_2} - T_0) = \\ \frac{T_2 \Big|_{x_2=l_2} - T_1 \Big|_{x_3=0}}{R_{th,1-2}/A_1} + \frac{1}{2} J_2^2 A_2 R_{C,1-2} = -\kappa_2 A_2 \frac{dT_2}{dx_2} \Big|_{x_2=l_2} + J_2 \alpha_2 A_2 T_2 \Big|_{x_2=l_2} + J_2^2 A_2 R_{C,1-2}. \end{aligned} \quad (25)$$

Here, heat transfer rate exiting the interface (the left side of the equation) also includes convection from the top surface of the electrode to the ambient. Similar analysis is performed at the electrode-sample interface, as stated in (26):

$$\begin{aligned} -\kappa_2 A_2 \frac{dT_2}{dx_2} \Big|_{x_2=0} + J_2 \alpha_2 A_2 T_2 \Big|_{x_2=0} = \frac{T_3 \Big|_{x_3=l_3} - T_2 \Big|_{x_2=0}}{R_{th,1-2}/A_1} + \frac{1}{2} J_3^2 A_3 R_{C,2-3} = \\ -\kappa_3 A_3 \frac{dT_3}{dx_3} \Big|_{x_3=l_3} + J_3 \alpha_3 A_3 T_3 \Big|_{x_3=l_3} + J_3^2 A_3 R_{C,2-3}. \end{aligned} \quad (26)$$

Finally, continuity of electrical current in the layers of the sample requires:

$$J_1 A_1 = J_2 A_2 = J_3 A_3 = J_4 A_4. \quad (27)$$

Modeling approach discussed above can be used to study in detail effects on temperature profile due to thermal and electrical properties of individual layers and contacts.

Thermal conductivity of the thermoelectric film is typically determined from relationship between temperature rise (usually the measured surface temperature) and dissipated power. In addition, difference between the surface and substrate temperature together with Seebeck voltage developed across the film is used to calculate Seebeck coefficient of the film. Practitioners in thermoelectric field need a way to evaluate steady state surface temperature before electrical current is switched off for transient Harman method under nonideal boundary conditions.

The main strategy pursued here is to use the superposition principle to calculate the total temperature rise by solving separately for temperature solutions under Joule heating and Peltier effects. Rather than using full set of Eqs. (21)–(27), several assumptions are made in this section in

order to arrive at an easy to use expression for the surface temperature, which still reflects the main thermoelectric transport mechanisms in many practical situations. These assumptions are: (1) electrode's contributions (layer 2) to thermoelectric transport are neglected because metallic electrode layers typically have low Seebeck coefficient similar to the probe and much lower electrical and thermal resistances compared to thermoelectric films; (2) Seebeck coefficient of the current probe is neglected; (3) convection terms on the film surfaces are neglected; (4) substrate thermal resistance and film-substrate electrode thermal contact resistances are neglected when compared to film thermal resistance, since thermoelectric film samples are typically low thermal conductivity films on high thermal conductivity substrates; and (5) Joule heating at film-substrate electrode contact is neglected because under assumption (4) the substrate acts as a heat sink.

Total temperature,  $T$ , in thermoelectric film is then divided into two components as:  $T = T' + T^*$ , where  $T'$  is linear temperature component, LTC, that is independent of Joule heating terms and includes Peltier effects, while  $T^*$  is nonlinear component, NLTC, and takes into account Joule heating effects, including electrical contact resistance heating. Then the set of Eqs. (21)–(27) for  $T'$  becomes:

$$-\kappa_3 A_3 \frac{d^2 T'_3}{dx_3^2} = 0, \quad (28)$$

$$T'_3 = T_0; x_3 = 0, \quad (29)$$

$$-\kappa_3 A_3 \frac{dT'_3}{dx_3} \Big|_{x_3=l_3} + J_3 A_3 \alpha_3 T'_s = \frac{T'_s - T'_w}{R_{th_{1-3}}/A_1} = q'_w; x_3 = l_3, \quad (30)$$

where  $T'_s$  and  $q'_w$  are temperature of the top surface of the sample and heat transfer rate through the probe, respectively. Heat transfer rate through the probe is calculated using a fin model with ambient temperature at free end and constant temperature  $T'_w$  at its base [16]:

$$q'_w = a(T'_w - T_0), \quad (31)$$

where the constant  $a$  is defined as:

$$a = \frac{\sqrt{h_1 P_1 \kappa_1 A_1}}{\tanh\left(\frac{l_1^2 h_1 P_1}{\kappa_1 A_1}\right)^{0.5}}. \quad (32)$$

Then, the solution for LTC of the top surface of the sample can be calculated as:

$$T'_s = \frac{(a_{th} l_3 / A_3 + \kappa_3) T_0}{a_{th} l_3 / A_3 + \kappa_3 - J_3 l_3 \alpha_3}, \quad (33)$$

where  $a_{th}$  is the total heat conductance through the contact and the probe defined as:

$$a_{th} = \frac{a}{1 + a R_{th_{1-3}} / A_1}. \quad (34)$$

Next,  $T^*$  is calculated from the following equations:

$$\frac{d^2 T_3^*}{dx_3^2} + \frac{J_3^2 \rho_3}{\kappa_3} = 0, \quad (35)$$

$$T_3^* = 0; x_3 = 0, \quad (36)$$

$$-\kappa_3 A_3 \frac{dT_3^*}{dx_3} \Big|_{x_3=l_3} + J_3 A_3 \alpha_3 T_3^* \Big|_{x_3=l_3} + J_3^2 A_3 R_{C-1-3} = \frac{T_S^* - T_w^*}{R_{th-1-3}/A_1} + \frac{1}{2} J_1^2 A_1 R_{C-1-2} = q_w^*; x_3 = l_3. \quad (37)$$

Heat transfer along the probe is calculated by solving the fin model with volumetric Joule heating and a temperature rise equal to zero (relative to the ambient) at free end of the fin (away from the sample). The equation for the probe heat transfer is:

$$q_w^* = aT_w^* - b, \quad (38)$$

where the constant  $b$  is expressed as:

$$b = -a \frac{J_3^2 A_3^2 \rho_1}{h_1 P_1 A_1} \left[ 1 - \frac{1}{\cosh[(l_1^2 h_1 P_1 / \kappa_1 A_1)^{0.5}]} \right]. \quad (39)$$

Then, the solution for NLTC is given by:

$$T_S^* = \frac{J_3^2 l_3 (R_{C-1-3} \frac{A_3}{A_1} + \frac{\rho_3 l_3}{2}) - \frac{l_3 b_{th} b_{cont}}{A_3}}{a_{th} l_3 / A_3 + \kappa_3 - J_3 l_3 \alpha_3}, \quad (40)$$

where,

$$b_{th} = \frac{b}{1 + aR_{th-1-3}/A_1} \quad b_{cont} = 1 + \frac{\frac{1}{2} J_3^2 \frac{A_3^2}{A_1} R_{C-1-3}}{b} \frac{aR_{th-1-3}}{A_1}. \quad (41)$$

Finally, total temperature of the top surface of the sample,  $T_s$ , is:

$$T_s = \frac{1}{a_{th} l_3 / A_3 + \kappa_3 - J_3 l_3 \alpha_3} \left[ \frac{(a_{th} l_3 / A_3 + \kappa_3) T_0 + J_3^2 l_3 (R_{C-1-3} \frac{A_3}{A_1} + \frac{\rho_3 l_3}{2}) - b_{th} b_{cont} \frac{l_3}{A_3}}{1} \right], \quad (42)$$

where the first term contains Peltier effect's induced contributions to the surface temperature, the second term includes Joule heating effects from the sample and contact, and the third term includes Joule heating contribution from the probe wire.

Temperature of the probe at junction with the sample surface is then calculated as:

$$T_w = \frac{T_S + \frac{R_{th-1-3}}{A_1} \left( \frac{1}{2} J_3^2 \frac{A_3^2}{A_1} R_{C-1-3} + aT_0 - b \right)}{1 + aR_{th-1-3}/A_1}. \quad (43)$$

Understanding how to eliminate or reduce the effects due to heat loss and electrical and thermal contact resistances is critical in designing test structures amenable for accurate

thermoelectric transport measurements. Parasitic effects are expected to be different for macroscale versus microscale samples, and this section focuses on microscale samples. To illustrate these effects, the surface temperature predictions as a function of current density are discussed for thermoelectric sample of  $10 \times 10 \times 10 \mu\text{m}^3$  in contact with copper probe of  $5 \mu\text{m}$  diameter and  $1.3 \text{ mm}$  length. Thermoelectric properties of thermoelectric film are similar to n-type  $\text{Bi}_2\text{Te}_{2.7}\text{Se}_{0.3}$  and are listed in **Table 2**.

	Probe	Sample	Electrode
Material	Cu	$\text{Bi}_2\text{Te}_{2.7}\text{Se}_{0.3}$	In
Lateral dimension ( $\mu\text{m}$ )	76.2 <sup>a</sup>	1014 <sup>b</sup>	1014 <sup>b</sup>
Length (mm)	20	1.8	0.05
Seebeck coefficient ( $\mu\text{V/K}$ )	1.84	-212	1.68
Thermal conductivity (W/m K)	401	1.5	82
Convection heat transfer coefficient ( $\text{W/m}^2\text{K}$ )	200 <sup>c</sup>	10	10
Electrical resistivity (nOhm m)	17.1	10500	84

a = Diameter, b = Width, c = The convection heat transfer coefficient for  $5 \mu\text{m}$  probe is  $3000 \text{ (W/m}^2\text{K)}$ .

**Table 2.** Sample parameters and thermal/thermoelectric properties. Reprinted from [21] with the permission of AIP Publishing.

**Figure 10** shows rise of surface temperature with respect to ambient temperature, calculated from Eq. (42) for a range of specific thermal contact resistances. Electrical resistance of contact was assumed to be equal to theoretical limit predicted for electrical boundary resistance between  $\text{Bi}_2\text{Te}_3$  and metal electrode [25]. Direction of electrical current was chosen such, that the sample surface undergoes Peltier cooling. At low current densities, Peltier cooling term dominates over Joule heating terms and temperature of the top surface of the sample decreases linearly as electrical current density increases. After reaching the maximum cooling temperature at optimum current density, Joule heating terms start to dominate over Peltier terms. Parasitic conduction heat transfer effect is apparent even at very low current densities, as shown by inset in **Figure 10**. It leads to reduction of temperature difference across the sample as compared to predictions of an ideal Harman model. On the other hand, as thermal contact resistance increases, the sample cooling is stronger because the thermal barrier created at the contact reduces heat transfer rate with the probe. Importance of thermal barrier effect is gauged by comparison between thermal resistances of the probe, probe-sample contact, and the sample itself. The modeled probe has thermal resistance of  $\sim 5 \times 10^4 \text{ K/W}$ , which is similar to  $6 \times 10^4 \text{ K/W}$  thermal resistance of the sample; therefore, a significant heat transfer occurs through the probe. As the thermal contact resistance increases, the probe heat transfer is reduced, particularly after contact thermal resistance becomes of the same order as thermal resistance of the probe. Alternative way to minimize the probe heat transfer rate could be realized by reducing diameter of the probe. However, besides practical challenges, this may have a negative impact associated with increase in resistance of electrical contact, as shown in **Figure 10**.

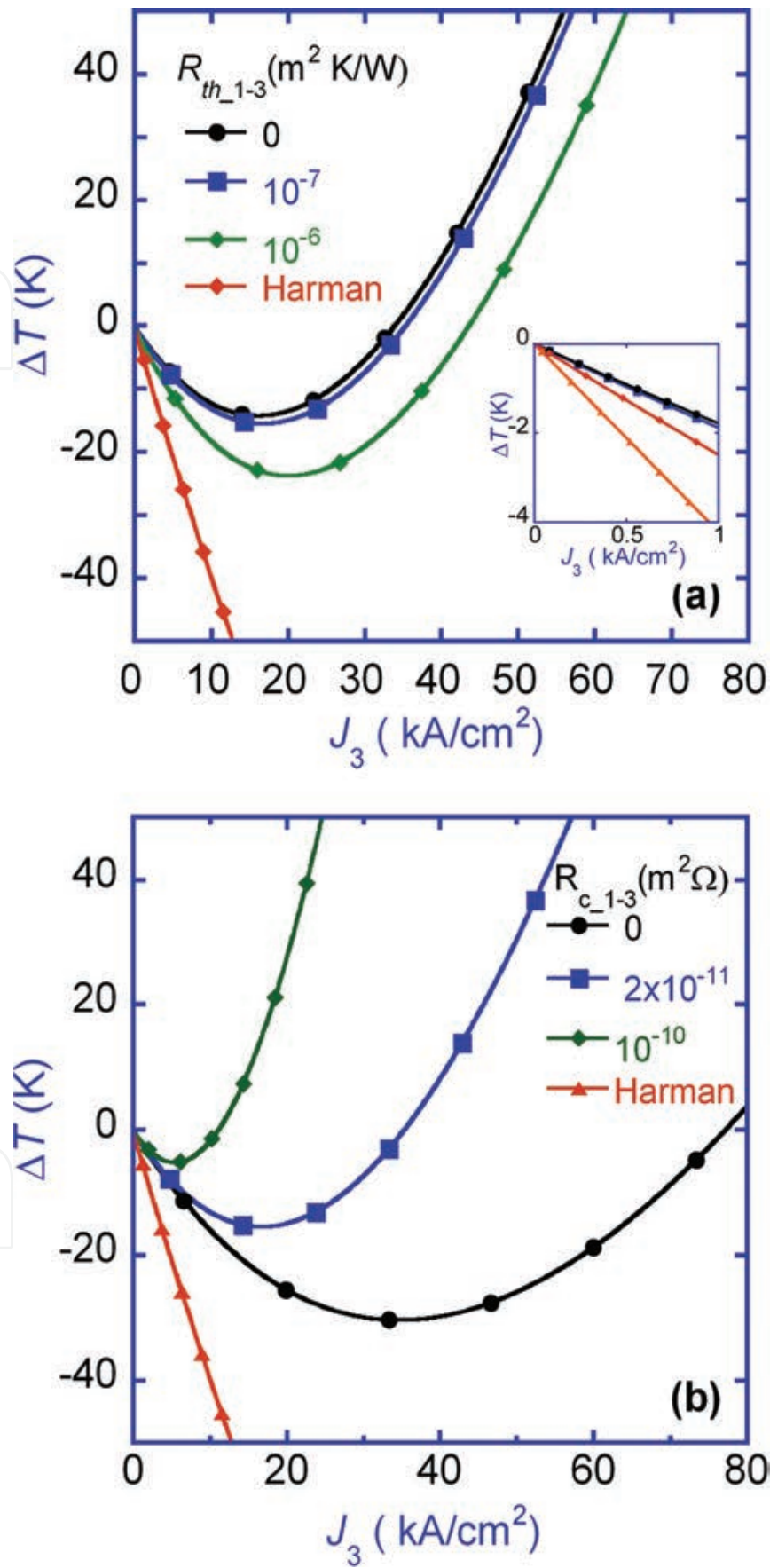


Figure 10. Calculated temperature response for specified  $R_{th}$  and  $R_c$ . Reprinted from [21] with the permission of AIP Publishing.

Heat transfer through the substrate could also play a major role in establishing the surface temperature. For large current densities, the strength of heat transfer through the substrate is indicated by large positive temperature difference measured across the sample. This difference is in contrast with the predictions of an ideal Harman model, where Joule heating effects never generate a temperature difference across the sample.

The effect of electrical contact resistance in absence of thermal contact resistance is investigated in **Figure 10**. The modeled probe has electrical resistance of  $\sim 1$  Ohm, which is similar to electrical resistance of the sample, therefore Joule heating effects can occur simultaneously in the sample and the probe. In addition, even for very low specific electrical contact resistance of  $1 \times 10^{-11}$  Ohm  $\times$  m<sup>2</sup>, electrical contact resistance for the modeled probe is considerable (0.5 Ohm). Electrical contact resistance increases by two orders of magnitude if the probe diameter is reduced by a factor of 10. This illustrates strong requirements to control the probe and contact electrical resistances in transient Harman experiments performed on film on substrate samples. This is because good thermoelectric samples have low electrical resistances, so Joule heating effect in contacts and probe can easily become dominant. Inspection of the probe and wire Joule heating terms suggests mitigation of the electrical contact resistance problem may be achieved by preparing thick film samples (large  $l_3$ ) for measurements, but with small cross-sectional area ( $A_3$ ) in order to increase the relative importance of electrical resistance of the sample. Since this strategy leads to an increase in thermal resistance of the sample, one must simultaneously address the need to mitigate parasitic probe heat conduction effects by choosing a probe with thermal resistance larger than that of the sample. The probe's thermal resistance may be calculated by knowing the material properties and diameter of the probe.

One proposed strategy for determining the properties under nonideal conditions is the bipolar method, where transient Harman experiments are performed using direct and reversed current directions and where measured Seebeck and resistive voltages across the sample are averaged. This is believed to eliminate Joule heating effects and reveal the intrinsic Peltier effects in the sample [21, 23]. However, as demonstrated in this work, when nonideal boundary conditions are present, parasitic effects cannot be always completely eliminated by this strategy. Nevertheless, the analysis below demonstrates the ability to exploit this behavior to determine both thermal and electrical transport properties of the samples and their contacts.

Bipolar resistive voltage difference measured across the sample  $\Delta V_{\rho\pm}$  is related to the total electrical resistance through the expression:

$$\frac{V_{\rho+} - V_{\rho-}}{J_3 A_3} = \frac{\Delta V_{\rho\pm}}{J_3 A_3} = 2 \left( R_{C_{1-3}}/A_1 + R_{C_{3-4}}/A_3 + \frac{\rho_3 l_3}{A_3} \right). \quad (44)$$

To find expression for bipolar Seebeck voltage, first Seebeck coefficient,  $\alpha_s$ , is expressed as measured  $V_s$  as a function of the surface temperature of the sample as:

$$\alpha_s = \frac{-V_s}{T_s - T_0}, \quad (45)$$

where  $V_s$  is experimental Seebeck voltage measured between the probe and electrode situated at the bottom of the sample. If the probe temperature is measured, then:

$$\alpha_S = \frac{-V_S}{(T_w - T_0) \left(1 + \frac{a_{R_{th,1-3}}}{A_1}\right) + \frac{R_{th,1-3}}{A_1} \left(b - \frac{1}{2} J_3^2 A_3^2 \frac{R_{C,1-3}}{A_1}\right)}. \quad (46)$$

When bipolar method is used, then  $\alpha_S$  can be extracted from bipolar Seebeck voltage difference  $\Delta V_{S\pm}$  and temperature difference  $\Delta T_{w\pm}$  using expression:

$$\alpha_S = \frac{-\Delta V_{S\pm}}{\Delta T_{S\pm}} = \frac{-\Delta V_{S\pm}}{\Delta T_{w\pm} \left(1 + \frac{a_{R_{th,1-3}}}{A_1}\right)}. \quad (47)$$

Next, under small current approximations:

$$\kappa_3 + a_{th} \frac{l_3}{A_3} \gg J_3 l_3 \alpha_3 \quad \& \quad T_0 \left(\kappa_3 + a_{th} \frac{l_3}{A_3}\right) \gg J_3^2 l_3 \left(R_{C,1-3} \frac{A_3}{A_1} + \frac{\rho_3 l_3}{2}\right) - \frac{l_3 b_{th} b_{cont}}{A_3}, \quad (48)$$

a simplified expression for bipolar surface temperature difference is obtained as:

$$\Delta T_{S\pm} = \frac{2T_0}{\kappa_3 + a_{th} l_3 / A_3} J_3 l_3 \alpha_3. \quad (49)$$

Expression for ZT obtained through bipolar technique is found as:

$$ZT_0 = \frac{-\Delta V_{S\pm}}{\Delta V_{\rho\pm}} \left(1 + \frac{a_{th} l_3}{\kappa_3 A_3}\right) \times \left(1 + \frac{R_{C,1-3} l_3}{\rho_3 A_3 A_1} + \frac{R_{C,3-4} l_3}{\rho_3 A_3^2}\right). \quad (50)$$

Another strategy is to perform experiments over a range of currents and use differential changes in  $V_S$  and  $V_\rho$  with current  $I$ . Under small current conditions, the following expression is then obtained for the figure of merit:

$$ZT_0 = \frac{-dV_S/dI}{dV_\rho/dI} \left(1 + \frac{a_{th} l_3}{\kappa_3 A_3}\right) \times \left(1 + \frac{R_{C,1-3} l_3}{\rho_3 A_3 A_1} + \frac{R_{C,3-4} l_3}{\rho_3 A_3^2}\right). \quad (51)$$

Neither bipolar nor differential current methods alone are able to account for all parasitic effects. As a result, these effects must be considered in data reduction or otherwise minimized. A variable thickness method [21, 23, 24] is used to account for electrical contact resistance effects, while heat losses and thermal resistance effects are neglected. A different method to determine all thermoelectric properties without the need for extensive sample preparations is outlined below.

The strategy explored here is to use bipolar experiments performed over a wide range of currents rather, than small current regime required by above methods. It is expected, that at large currents, experimental Seebeck voltage and temperature signals become sensitive to electrical transport properties of the sample and contacts and could be used to determine the sample and contact thermoelectric properties. In addition to Seebeck and resistive voltage

drops, method requires measurement of the sample surface temperature or the probe temperature (at the contact with the samples surface).

Proposed strategy takes into consideration selective sensitivity of thermal signals to Peltier and combined Peltier and Joule heating effects under low and high current regimes, respectively. Under small current approximations, temperatures of the probe and sample surface are linear with current, and thermal conductivity can be expressed as a function of experimentally measured slope of the probe temperature as:

$$\kappa_3 = \frac{l_3}{A_3} \left[ \frac{\alpha_3 T_0}{\left(1 + \frac{aR_{th,1-3}}{A_1}\right) dT_w/dI} - a_{th} \right]. \quad (52)$$

In Eq. (52), value of Seebeck coefficient is substituted from Eq. (47), which is valid at any current. Next, Eqs. (44), (47), and (52) are substituted in Eq. (43). For the sake of discussion it is assumed, that specific electrical contact resistance is similar at the top and bottom contacts (other assumptions are discussed in Section 3). After the above substitutions, predicted probe temperature and Seebeck coefficient become a function of two unknowns, specific electrical and thermal contact resistances, which are then used to fit experimental signals under large current regime for both direct and reverse currents. This strategy allows the unique determination of all thermoelectric properties of the sample and electrical and thermal contact resistances. Details of the fitting procedure are presented in experimental validation section.

### 2.3.2. Lock-in Harman technique—analytical model

To find *frequency-dependent* temperature solution in the sample, governing equation and boundary conditions for the problem were first expressed as a function of time and then transformed to frequency domain. Governing thermal transport equation for the sample with attached wires was derived by balancing the energy in infinitesimal length  $dx$  of wire or sample domain treated as Joule heated fin and neglecting Thompson effects. Approach is similar to the steady state model [25]. The governing equation is:

$$\frac{\partial^2 T_i(x, t)}{\partial x_i^2} - m_i^2 (T_i - T_0) + \frac{J^2 \rho_i}{2\kappa_i} = \frac{1}{\Delta_i} \frac{\partial T_i(x, t)}{\partial t}. \quad (53)$$

The first term on the left side accounts for conduction through the wire/sample, where  $T_i$  is temperature along length of the wire/sample as a function of position,  $x$ , and time,  $t$ . The second term represents convective heating or cooling from the environment, where  $m_i^2 = h p / (\kappa A)$ , with  $h$  being heat transfer coefficient,  $p$  wire/samples circumference,  $A$  its cross-sectional area, and  $T_0$  ambient temperature. The third term accounts for Joule heating, and the right side of equation is transient heat storage term.  $J$  is electrical current density, and  $\Delta$  is thermal diffusivity.

**Figure 11** represents the same configuration of sample and wires as considered before, but here shows heat transfer domains used in the model. 1D heat transfer was modeled in each of

seven domains, one each for the six wires plus another for the sample. Details of the boundary conditions are given below. Temperature solution requires a total of 14 boundary conditions, two for the sample and four for each set of wires. The wire boundary conditions are as follows: two boundary conditions per wire (or six total) were defined by assuming, that the end of each wire was at room temperature, since the wires in the experiment were relatively long compared to their width and measurements were conducted in ambient conditions. The remaining two boundary conditions per wire (summing to twelve in total) are that the ends of each wire in contact with the sample are at a fixed temperature. The two boundary conditions across the sample come from the fact, that heat transfer at the interfaces must be balanced. For the interface between the first set of wires (domains 1–3) and the sample (domain 4), the energy balance yields Eq. (54):

$$q_{1-3} + J_4^2 A_4 R_{14} + J_4 \alpha_{34} A_4 T_4(0, t) = -\kappa_4 A_4 \frac{\partial T_4(0, t)}{\partial x_4} \quad (54)$$



**Figure 11.** Schematic representation of the sample showing heat transfer domains.

The first term is the rate of heat conduction to and from the wires and is a function of temperature gradient at the wire-sample interface and thermal conductivity of the wires. This is calculated using the pin fin equation below for the experimental results. The second term accounts for Joule heating due to electrical contact resistivity between the current lead and the sample,  $R_{14}$ . The third term is Peltier heating at the interface, where  $\alpha_{34} = \alpha_3 - \alpha_4$ , relative Seebeck coefficient between the wire (3) and the sample (4). The right side of the equation is the heat conducted through the sample. Form of boundary condition for the other wire-sample interface is identical. To transform the problem from a partial differential equation in time to an ordinary differential equation in frequency,  $\omega$ , we used Fourier transform. Before applying Fourier transformation, it was convenient to represent the sample temperature as a Fourier series. This was possible since temperature is a function of periodic excitation signal and is therefore itself periodic. Temperature as the sum of its DC component ( $\eta = 0$ ) and all of the harmonics (all other values of  $\eta$ ) of fundamental frequency,  $\omega_0$ , is given by Eq. (55):

$$T_i(x, t) = \sum_{-\infty}^{\infty} T_i(x, n\omega_0) e^{i\eta\omega_0 t}. \quad (55)$$

Substituting this into governing equation and applying Fourier transform gives transformed governing equation:

$$\frac{\partial^2 T_i(x, \omega)}{\partial x_1^2} - m_i^2 T_i(x, \omega) + m_i^2 T_0 \sqrt{2\pi} \delta(\omega) + \frac{J^2 \rho_i}{8\kappa_i} \sqrt{2\pi} (2\delta(\omega) + \delta(\omega - 2\omega_0) + \delta(\omega + 2\omega_0)) = \frac{i\omega}{\Delta_i} T_i(x, \omega). \quad (56)$$

Dirac delta function,  $\delta$ , is employed because signals of constant frequency in the time domain become delta functions in frequency domain. Conduction, convection, and heat storage terms are present at each harmonic with additional convection term present at  $\omega = 0$ . Joule heating occurs only at  $\omega = 0$  and  $\omega = 2 \cdot \omega_0$ . The transformation was next applied to the boundary conditions. The transformed boundary condition for the first interface is given by Eq. (57):

$$q_{1-3} + \frac{J_4 A_4 R_{14}}{2} \sqrt{2\pi} (2\delta(\omega) + \delta(\omega - 2\omega_0) + \delta(\omega + 2\omega_0)) + \frac{J_4 S_{34} A_4}{2} \sum_{-\infty}^{\infty} T_4(0, n\omega_0) \sqrt{2\pi} (\delta(\omega - \omega_0(n + 1)) - \delta(\omega - \omega_0(n - 1))) = -\kappa_4 A_4 \frac{\partial T_4(0, \omega)}{\partial x_4}. \quad (57)$$

Joule heating term is again present at  $\omega = 0$  and  $2 \cdot \omega_0$ , while Peltier heating term occurs only at the fundamental frequency. This demonstrates mathematically how Joule and Peltier components of heat transfer are separated by measuring the harmonics of temperature. All measurements in this work use Peltier component. Joule component is not used in measurements described here. Since this work focuses on the first harmonic measurements, the solution for the first harmonic and its derivative are given by Eq. (58) and Eq. (59), where  $R$  is the root of homogenous form of governing equation and is given by Eq. (60):

$$T_i(x_i, \omega) = c_{i1,1\omega} e^{R_{1\omega} x} + c_{i2,1\omega} e^{-R_{1\omega} x}, \quad (58)$$

$$\frac{\partial T_i(x_i, \omega)}{\partial x_i} = c_{i1,1\omega} R_{1\omega} e^{R_{1\omega} x} - c_{i2,1\omega} R_{1\omega} e^{-R_{1\omega} x}, \quad (59)$$

$$R = \sqrt{m^2 + \frac{i\omega}{\Delta}}. \quad (60)$$

The undetermined coefficients were solved numerically using transformed boundary conditions.

### 2.3.3. Experimental results—transient Harman

**Figure 12** shows experimentally measured total and Seebeck voltages as a function of current.

Resistive voltage drop obtained after subtracting Seebeck voltage from total voltage includes contributions from the sample, probe-sample contact, and sample-substrate electrode contact. Inset in **Figure 12** shows an example of measured voltage as a function of time during an experiment at 163 mA. The figure of merit calculated according to classical Harman method

yields an average value of 0.11, much smaller than the manufacturer value of 0.85. This discrepancy is due to parasitic effects neglected in classical technique.

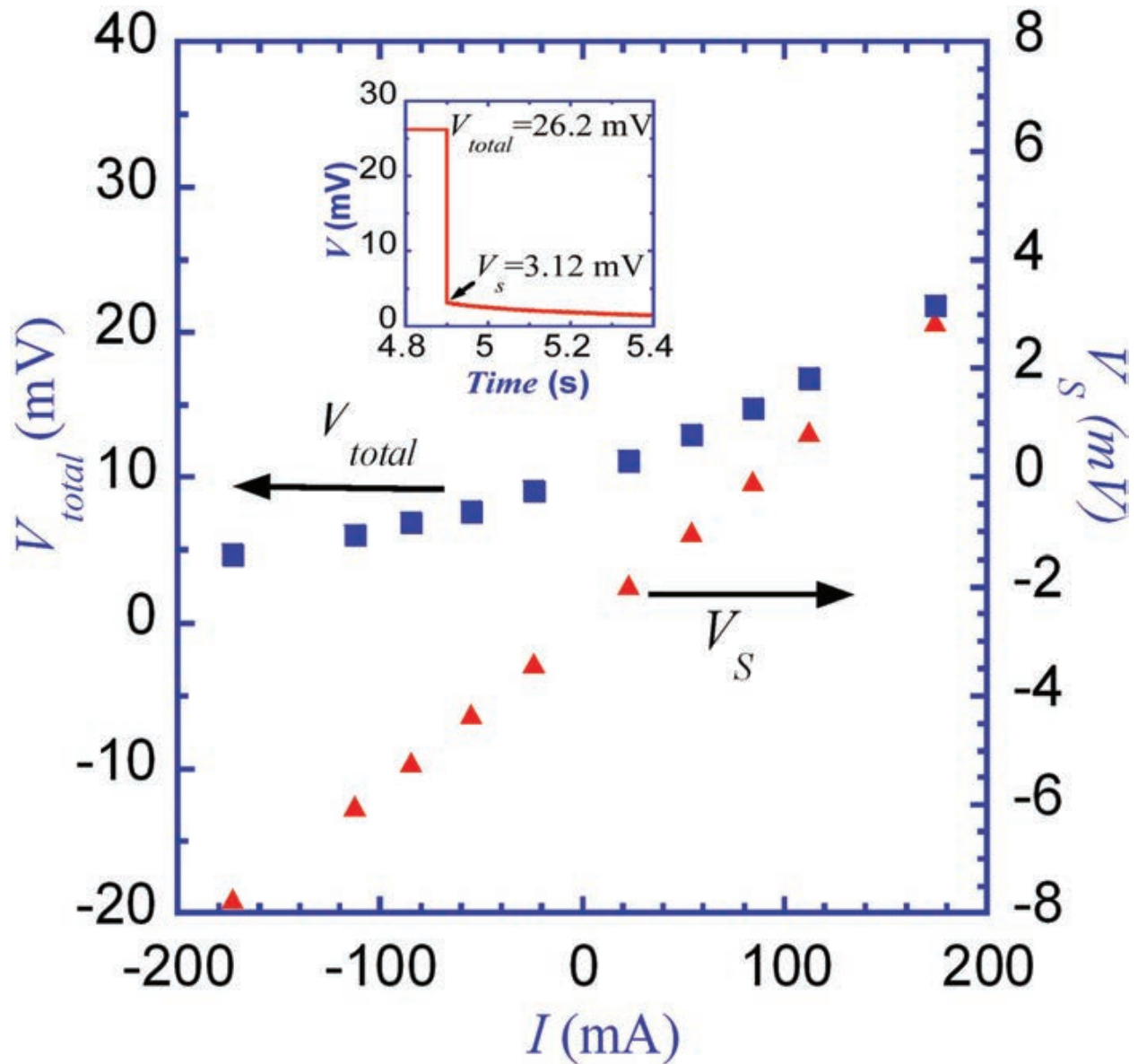


**Figure 12.** The deconvolution of resistive and Seebeck voltage contributions. Reprinted from [21] with the permission of AIP Publishing.

Measured probe temperature is linear with current for the smallest two bipolar currents and yields a slope of  $-55.1$  K/A and was substituted in Eq. (52). Originally, only one probe was modeled in contact with the sample, the energy loss across constantan wire was evaluated and found to be in an order of magnitude smaller than for copper wire, therefore its effect is expected to be negligible.

Transient Harman experiments performed under the highest direct and reverse current conditions were used in the fitting of sample's thermoelectric properties and contact resistances. In the fitting procedure, thermal contact resistance  $R_{th,1-3}$  was varied over a wide range, typically

between  $1.0 \times 10^{-8} \text{ m}^2 \times \text{K/W}$  and  $1.0 \times 10^{-5} \text{ m}^2 \times \text{K/W}$  with step of  $1.0 \times 10^{-8} \text{ m}^2 \text{ K/W}$ . For each  $R_{\text{th},1-3}$  value, sample's Seebeck coefficient was determined from Eq. (47) and sample's thermal conductivity was determined from Eq. (52). In addition, two sets of solutions for electrical contact resistance as function of  $R_{\text{th},1-3}$  are generated by fitting experimental Seebeck coefficient and the probe temperatures. The first set of solutions is obtained by minimizing the mean square deviation between Seebeck coefficient values calculated from Eqs. (46)–(47). The second set of solutions is obtained by minimizing the mean square deviation between experimental temperatures of the probe and the predictions of Eq. (43). In Eq. (43),  $T_s$  was substituted from Eq. (42), thermal conductivity was substituted from Eq. (52), Seebeck coefficient from Eq. (47) and resistivity of the sample from Eq. (41). It was found, that the first set of solutions is more sensitive to thermal contact resistance, while the second set was more sensitive to electrical contact resistance. The intersection of the two sets of solutions leads to the unique solution for thermal and electrical contact resistances and thermoelectric properties of the sample.

Since the original sample-substrate interface from commercial Peltier device has a negligible electrical contact resistance compared with the sample,  $R_{\text{C},3-4}$  was taken as zero in Eq. (41). It was also assumed, that  $R_{\text{c},1-3}$  and  $R_{\text{th},1-3}$  represent respectively lump electrical and lump thermal contact resistance contributions due to the probe-indium interface, indium layer (negligible contribution), and indium-sample interfaces. However, measured resistive voltage drop through the constantan probe does not include electrical resistance contribution due to the probe-indium interface. Therefore, the fitting procedure was repeated several times under four different assumptions regarding contact electrical resistance. The assumptions and the fitting results are presented and discussed below.

The thermoelectric properties arise from each of the following four cases are summarized in **Table 3**. In case 1, electrical contact resistance  $R_{\text{c},1-3}$  was assumed to originate only from the probe-indium interface. In case 2, electrical contact resistance  $R_{\text{c},1-3}$  was assumed to originate only from the indium-sample interface. In case 3, electrical contact resistance  $R_{\text{c},1-3}$  was assumed to split equally between probe-indium and indium-sample interfaces. Finally, in case 4, manufacturer's value for sample resistivity  $\rho_3 = 1 \times 10^{-5} \text{ Ohm} \times \text{m}$ , was used in the fitting process, which allowed the exact determination of the split of probe-sample electrical contact resistance between two contributions. In this case,  $R_{\text{c},1-2} = 4.9 \times 10^{-10} \text{ Ohm} \times \text{m}^2$  may be split as  $1.1 \times 10^{-10} \text{ Ohm} \times \text{m}^2$  due to the probe-indium interface and  $3.8 \times 10^{-10} \text{ Ohm} \times \text{m}^2$  due to indium-sample interface. Relatively large values of measured electrical and thermal contact resistances are due to the imperfections of the mechanical contact under the small contact load used in this proof-of-concept experiment. The indium-pellet interface dominates the contact resistance.

The highest deviations between measured sample's Seebeck and thermal conductivity as compared with manufacture's values are respectively  $6 \text{ } \mu\text{V/K}$  (3%) and  $0.12 \text{ W}/(\text{m} \times \text{K})$  (8 %). These deviations are smaller than the experimental uncertainty. The uncertainty in thermal conductivity due to propagation of the uncertainty in temperature and voltage measurements was calculated to be  $0.26 \text{ W}/(\text{m} \times \text{K})$ . Similarly, for Seebeck coefficient, the uncertainty is equal to  $9.9 \text{ } \mu\text{V/K}$ . To accurately determine the sample resistivity, resistive voltage drop should be

measured through the copper probe, which is used to pass electrical current, at the same time as through the constantan wire, so total electrical contact resistance and sample resistivity can be accurately determined. When correct resistivity of the sample was employed in the fitting, the sample thermal conductivity was within 3 % of manufacture's values.

Case #	$R_{th,1-3}$ (K/W)	$\kappa_3$ (W/mK)	$\alpha_3$ ( $\mu$ V/K)	$R_{c,1-3}$ ( $m^2$ Ohm)	$\rho_3$ (Ohm m)
1	$1.1 \times 10^{-6}$	1.38	-212	$2.9 \times 10^{-10}$	$5.7 \times 10^{-5}$
2	$6.6 \times 10^{-7}$	1.48	-218	$6.2 \times 10^{-10}$	Nonphysical (negative)
3	$9.4 \times 10^{-7}$	1.43	-215	$3.9 \times 10^{-10}$	$3.3 \times 10^{-5}$
4	$7.8 \times 10^{-7}$	1.46	-217	$4.9 \times 10^{-10}$	$1 \times 10^{-5}$ (manufacturer specified)

**Table 3.** Summary of cases simulated to explore effect of contacts in transient Harman measurements.

**Figure 13** shows comparison between measured and calculated temperature of the probe as a function of electrical current passed through it.

The theoretical predictions use the fitted thermoelectric properties and employ Eq. (43) with either all terms or only Peltier terms. The theoretical predictions were performed for all cases 1–4 and, since they superpose along the same line, they are not individually distinguishable in **Figure 13**. Joule heating effects are important at large currents in tested sample, as demonstrated by the discrepancy between Peltier heating only predictions and combined Peltier and Joule heating model. Predictions based on solving Eq. (20)–(27), that also include the convection on the sample surface and the contributions from indium electrode, show no significant difference with prediction based on Eq. (43). There is an excellent agreement between experimental and modeling data over entire electrical current range. Data sets for intermediate current values ( $\sim 85$  mA) show also excellent agreement, although they have not been used in the fitting.

#### 2.3.4. Experimental results—lock-in Harman

ZT and individual thermoelectric properties may also be characterized experimentally using a Nyquist plot (plotting imaginary vs real parts of the complex voltage signal or sample temperature rise). Nyquist analysis of voltage measurements across the sample allows for direct calculation of the slope  $m$ , which, in turn, yields  $\alpha$ . ZT is obtained from finding each of  $V_R$  and  $V_S$  from the different regimes represented in the plot (see **Figure 14**).  $V_R$  is obtained from the value of the real part of the voltage response when the imaginary part is equal to zero, and  $V_S$  is the radius of the circular portion of the Nyquist plot.

The samples measured were bulk bismuth telluride alloys with dimensions of  $4.5 \times 3.8 \times 3.8$  mm<sup>3</sup>. Thin layer of gold was deposited on either end to improve adhesion and current spreading between the sample and lead wires. One lead wire and one thermocouple were soldered to either end of the sample. Current was applied through un-insulated 50.8  $\mu$ m diameter copper wire, and voltage was measured using 50.8  $\mu$ m E-type thermocouples. Two sets of voltage measurements were made across the sample using each set of thermocouple

wires for excitation frequencies between 10 mHz and 10 Hz. Amplitudes of resulting voltages,  $E_{13}$  and  $E_{24}$ , are plotted in **Figure 14**. When the signal is applied at low frequencies, then measured voltage is sum of total voltage across the sample and Seebeck voltage in thermocouple's wires. As frequency is increased, thermal component in the sample and wires decays and voltage approaches resistive voltage of the sample, and  $E_{13}$  approaches  $E_{24}$ .

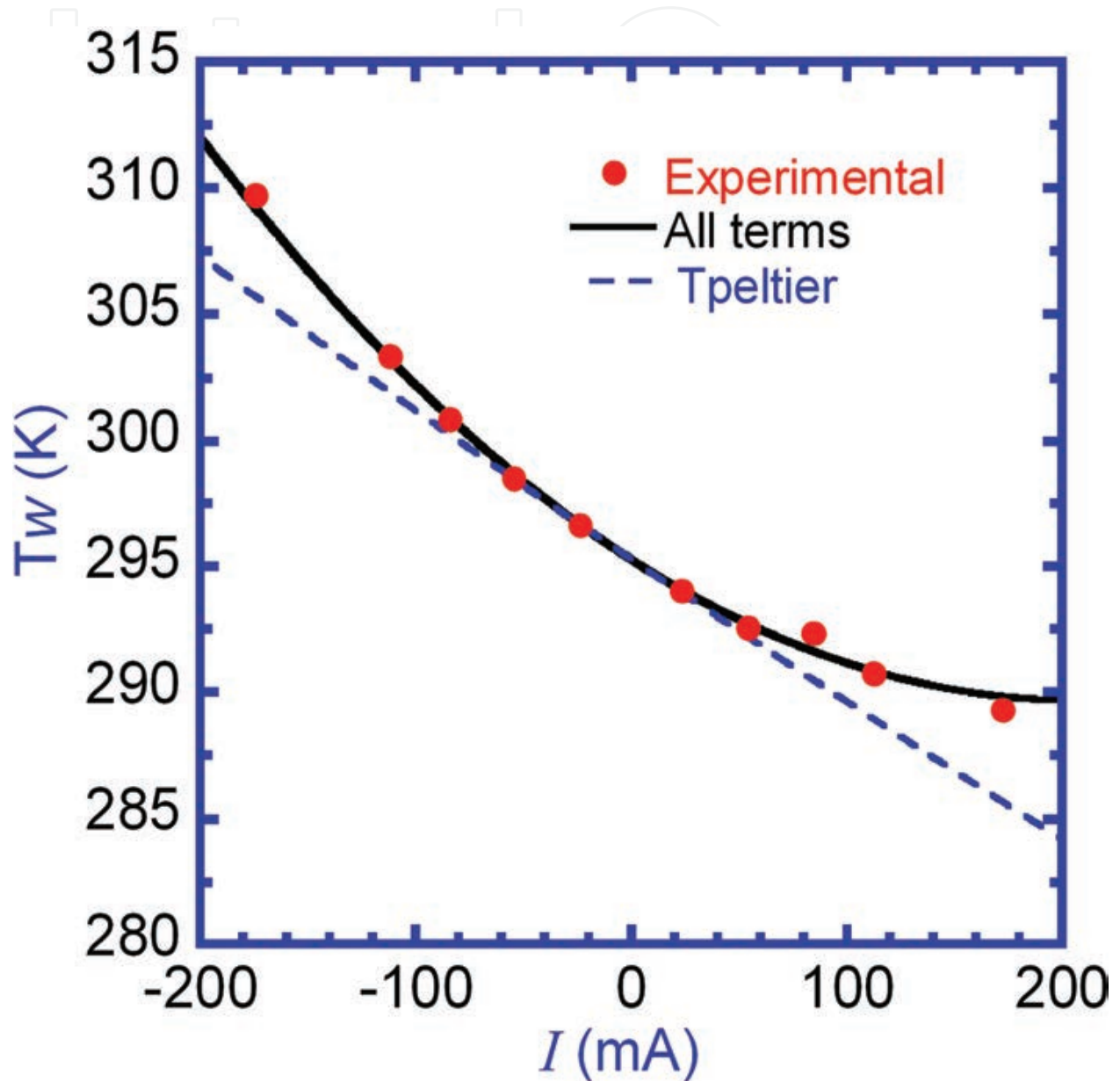


**Figure 13.** Measured versus calculated probe temperature. Reprinted from [16] with the permission of AIP Publishing.

These two voltages were used to find Seebeck coefficient by Ivory's technique [22] using Eq. (21). Non-imaginary values of two voltages are plotted against each other in **Figure 15** and resulting in Seebeck coefficient  $\alpha_{\text{sample}} = 202.6 \pm 1.4 \mu\text{V/K}$ . Real parts of signals are used, as these are components, that are in phase with excitation signal and as a result are in phase with each other. Amplitudes may be out of phase with each other and imaginary part is much

smaller. Advantage of Ivory technique is that the magnitudes of measured voltages are greater than in traditional technique, if  $\alpha_{\text{sample}}$  is larger than average value of  $\alpha_a$  and  $\alpha_b$ , which is often the case, when measuring thermoelectric materials, because voltage measured across the sample is equal to  $\Delta T(\alpha_a - \alpha_{\text{sample}})$ , whereas that measured in thermocouples is  $\Delta T(\alpha_a - \alpha_b)/2$ . This assumes, that the sample is symmetric and that  $\Delta T$  is total temperature gradient across the sample. Thus, temperature gradient measured by one set of thermocouples is  $\Delta T/2$ . Since temperatures on the two sides of the sample are  $180^\circ$  out of phase, the total temperature difference is twice the temperature amplitude registered on one side. The larger signal results in better signal-to-noise ratios and less error in the final calculation.

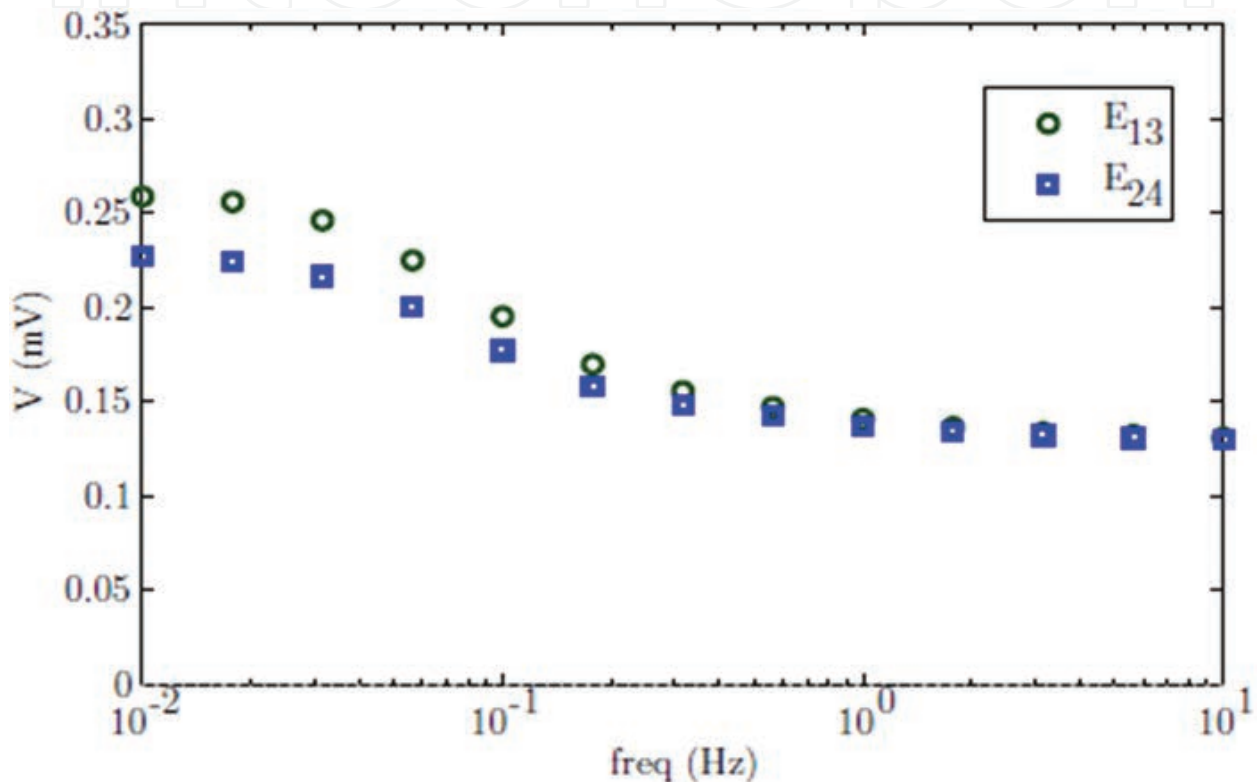


Figure 14.  $E_{13}$  and  $E_{24}$  voltages as a function of frequency.

Total voltage in the sample  $V_{\text{sample}}$  was calculated using Eq. (61) and then plotted on Nyquist diagram, shown in **Figure 16**:

$$V_{\text{sample}} = \frac{\alpha_b E_{13} - \alpha_a E_{24}}{\alpha_b - \alpha_a}. \quad (61)$$

Obtained data is again shown as superposition of resistive  $V_R$  and Seebeck  $V_S$  voltages, and  $V_{\text{sample}}$  and  $V_R$  can be found by extrapolating the data to the real axis as described in introduction. High frequency behavior of real devices may not obey the  $-45^\circ$  assumption, if contacts have significant heat capacity [25]. As seen in **Figure 16**, behavior of the sample deviates somewhat from  $-45^\circ$ , which can be attributed to heat capacity of the solder between the wires and the sample. From **Figure 16**,  $V_{\text{sample}}$  is 0.17 mV and  $V_R$  is 0.088 mV. Extrinsic ZT of the device is 0.93 for this measurement. To find intrinsic ZT of the material, then nonidealities in measurement system must be accounted for.

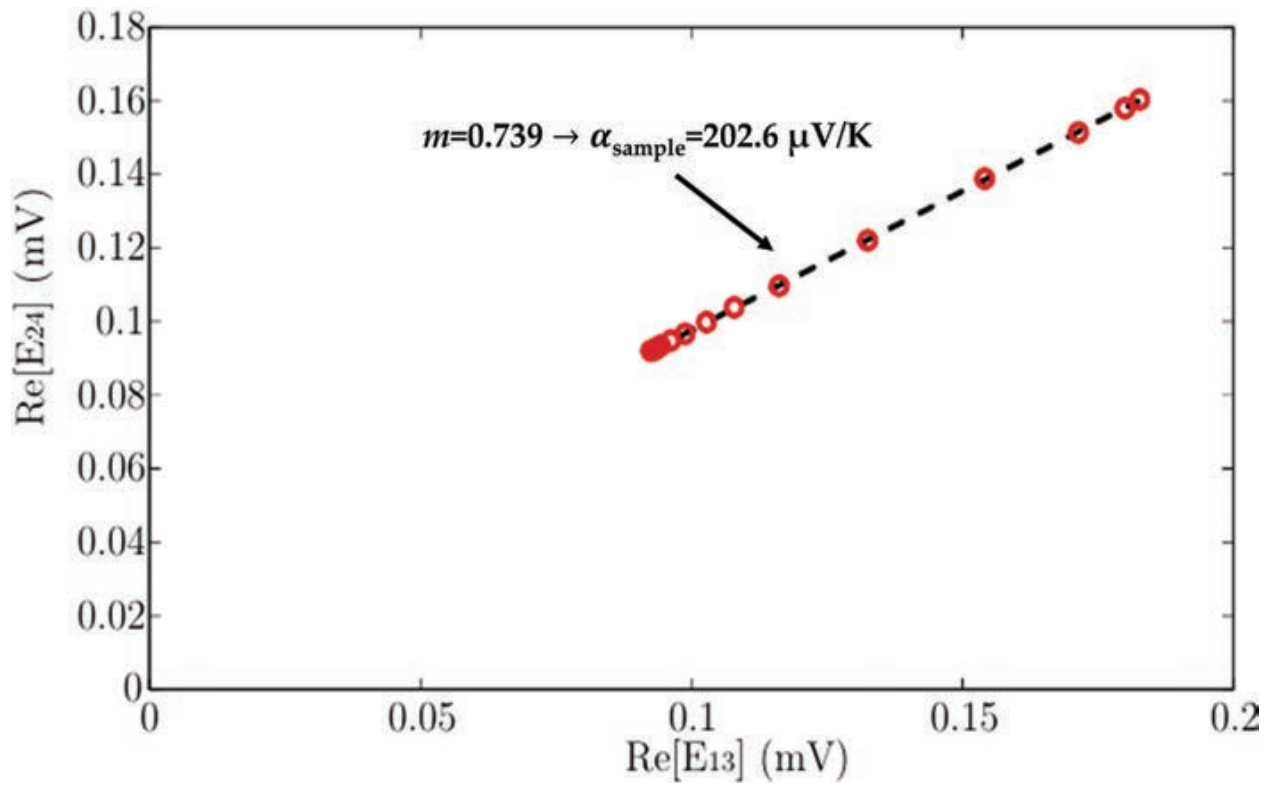


Figure 15. Real parts of  $E_{24}$  and  $E_{13}$  to find the slope,  $m$ , and Seebeck coefficient.

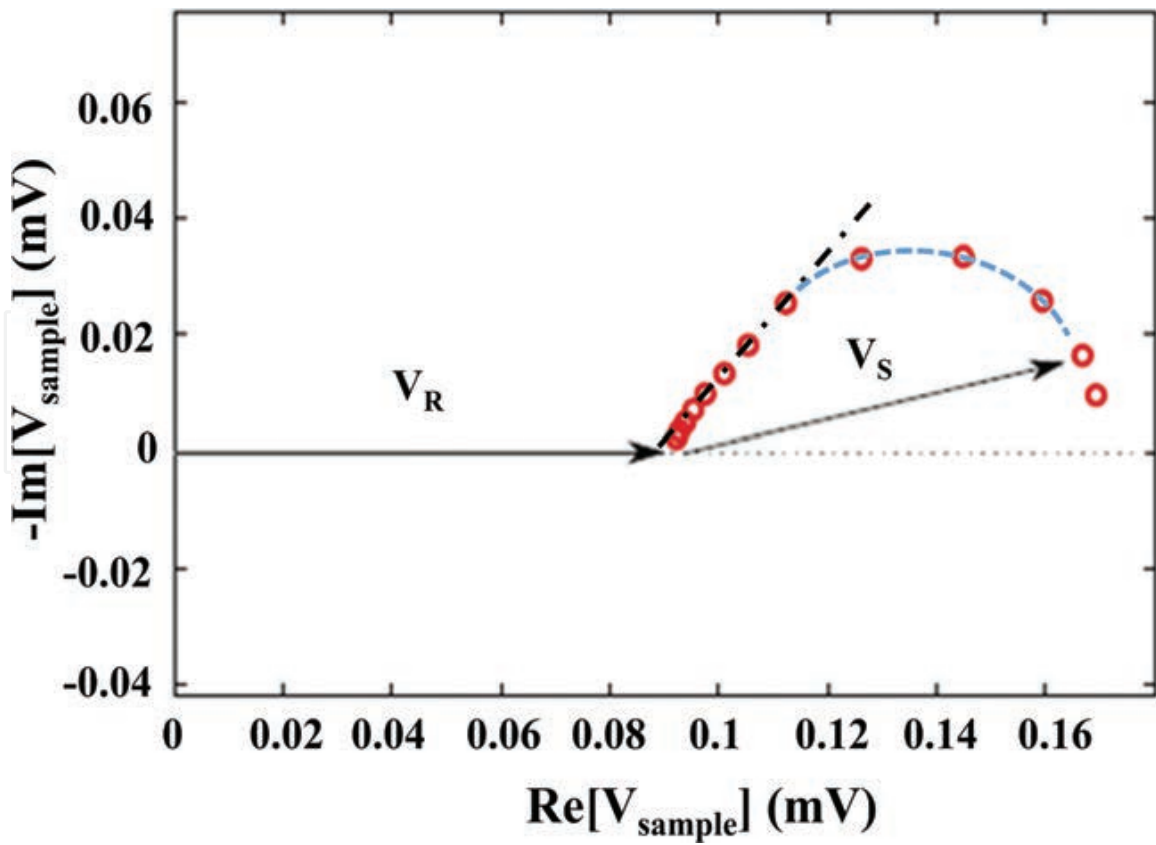


Figure 16. Voltage measurements plotted on Nyquist diagram.

To find equation for intrinsic ZT, the derivation of ZT performed by Harman can be repeated to include terms for heat loss and contact resistance. This adds two correction factors as shown in Eq. (62). The first is the ratio of heat lost from the sample to Peltier heat generation at the wire-sample interface. This heat loss may be due to either convection or radiation from the end of the sample or conduction through the contacts. The second correction factor is the ratio of voltage drop across the contacts to that in the sample, which is equal to resistance of the contacts divided by that of the sample:

$$ZT = \frac{V_S}{V_R} \left[ \left( 1 - \frac{q_{\text{loss}}}{q_{\text{Peltier}}} \right) \left( 1 - \frac{V_C}{V_R} \right) \right]^{-1}. \quad (62)$$

For this experiment, radiation and convection from the sample itself were negligible compared to heat loss through the contacts and only the latter was considered. Since ZT was calculated using voltages approximating DC, where heat transfer is in steady state, and high frequency AC, which is not affected by heat losses, steady-state equation can be used to account for heat loss. Conduction through the wires is described by Eq. (63), which is the fin equation, where the base temperature is equal to that of the wire-sample interface,  $T_s$ , and  $T_0$  is the ambient temperature:

$$q_w = \sqrt{hp\kappa A}(T_s - T_0) \tanh \left( \sqrt{\frac{hP}{\kappa A}} L \right). \quad (63)$$

For long thin wires, the hyperbolic tangent goes to one and may be neglected. We considered losses by convection through the wire and temperature at the end of the wire away from the sample was assumed to have reached ambient (since wires were long and thin). Even though, the sample temperature was not measured directly, the temperature gradient across the sample was found from measured Seebeck coefficient value,  $\alpha_{\text{sample}}$ , and Seebeck voltage,  $V_S$ . Once  $T_s$  was found this way and substituted in Eq. (63),  $q_w$  was determined for each of two wires, summed up and the value used in Eq. (62). In the equation,  $q_{\text{Peltier}} = aIT$ . After all these substitutions, intrinsic ZT of the material was calculated as 1.04.

Samples resistivity was determined as  $7.0 \times 10^{-6}$  Ohm  $\times$  m based on resistive voltage,  $V_R$ , and neglecting the contribution of the contacts. This was confirmed in independent measurement probing resistive voltage profile along the length of the sample, which resulted in value of  $7.25 \times 10^{-6}$  Ohm  $\times$  m. Using intrinsic ZT, measured Seebeck coefficient and the first value of resistivity, thermal conductivity of 1.55 W/(m  $\times$  K) is obtained, while if the second resistivity value is used  $\kappa$  is determined as 1.6 W/(m  $\times$  K).

The same material properties were also found by fitting the predictions based on the numerical model described above in Eqs. (58)–(60) to experimental data. The fitting is shown in **Figure 17**, where Seebeck voltage data was converted to temperature amplitude using measured Seebeck coefficient. Adjusting thermal conductivity in the model and using the least squares fit, thermal conductivity was 1.55 W/(m  $\times$  K) and thermal diffusivity was  $9.5 \times 10^{-3}$  cm<sup>2</sup>/s.

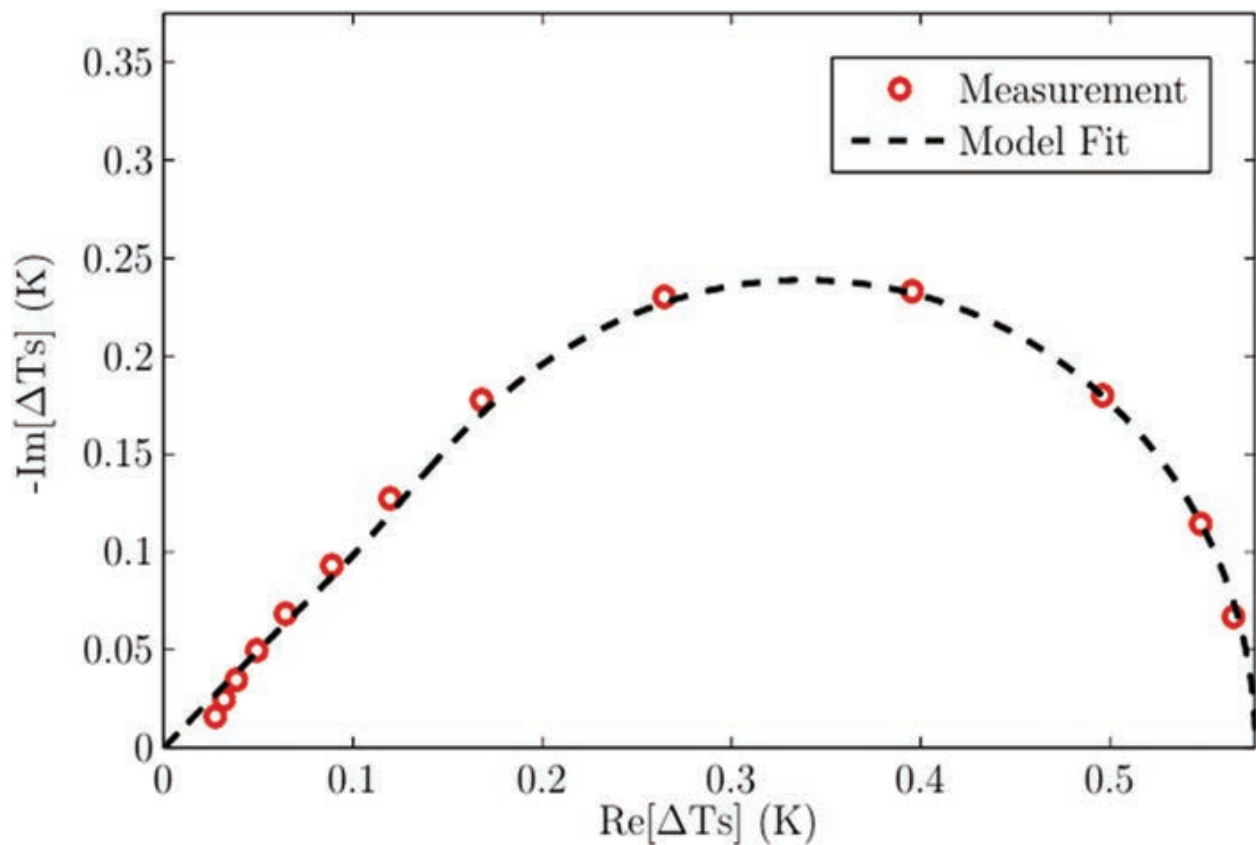


Figure 17. Sample temperature and fitted prediction plotted on Nyquist diagram.

Overall, calculated uncertainty in this experiment was small with that in Seebeck coefficient and extrinsic ZT measurements being lower, than that of calculated intrinsic ZT. The latter is due to the uncertainty in calculating the heat loss through the wires, specifically calculating the heat transfer coefficient between the wires and the air. The heat transfer coefficient was calculated assuming a horizontal cylinder in air. While the uncertainty for the heat transfer coefficient was determined to be about 2%, its uncertainty was assumed to be closer to 10%. This was done because there is some additional uncertainty surrounding the assumptions of free convection and due to its dependence on lab conditions. The uncertainty could be improved by testing the sample in an evacuated chamber, eliminating entirely the need to calculate heat transfer coefficient. The uncertainty of extrinsic ZT is due to that of voltage measurements, and was assumed to be 1% of the measured value, and temperature, assumed to be  $296 \pm 2$  K. The uncertainty in voltage measurement was assumed 1% as conservative estimate. The error of the device was lower, but noise in the system and variation between measurements was closer to 1%. Some error in Seebeck coefficient measurement will be present due to the assumption, that temperature gradients across all the wires in each thermocouple are identical. Since the junctions of thermocouples were somewhat embedded in solder, there may be slight temperature gradient between two wire-solder interfaces. However, this difference was assumed to be negligible compared to temperature gradient along lengths of wires, and the uncertainty in Seebeck coefficient measurement was calculated as less than 1%. The uncertainty in  $V_{\text{sample}}$  was similarly low, while that in determining  $V_R$  from the sample voltage was calculated to be about 2–3%.

These were calculated using error propagation from the uncertainty of the measurements. For extrinsic value of ZT, the uncertainty was calculated as 2.7%. With addition of the uncertainty in the heat loss calculation, that for intrinsic ZT increased to 5.9%.

### 3. Verification strategies for measurements

#### 3.1. Slope-efficiency method: rapid measurement of device $ZT_{\text{maximum}}$

Maximum electrical power output,  $P_{\text{max}}$ , of any thermoelectric generator (TEG) depends on open-circuit voltage,  $V_{\text{oc}}$ , and occurs when internal device resistance,  $R_{\text{int}}$ , exactly equals to resistance of external load. When  $R_{\text{int}} = R_{\text{load}}$ , then total system resistance =  $2R_{\text{int}}$  and  $V_{\text{oc}}$  drops exactly by half leading to:

$$P_{\text{max}} = \frac{V_{\text{oc}}^2}{4R_{\text{int}}}. \quad (64)$$

For TEG consisting of some number “ $i$ ” of individual “thermocouples” connected in series and each having n-type thermoelement and p-type thermoelement, Seebeck effect relates  $V_{\text{oc}}$  to the temperature difference,  $\Delta T$ , induced by the heat source as described:

$$V_{\text{oc}} = \sum_0^i (\alpha_n + \alpha_p)_i \Delta T, \quad (65)$$

where  $\alpha_n$  and  $\alpha_p$  are values of n-type and p-type Seebeck coefficients from each individual thermoelement, respectively. Thus, the sum of Seebeck coefficients from  $i$  thermocouples is ensemble-average proportionality between  $V_{\text{oc}}$  and  $\Delta T$ . Likewise,  $R_{\text{int}}$  is the sum of resistances from  $i$  thermocouples, and it is the ensemble-average electrical resistivity of n-type ( $\rho_n$ ) and p-type ( $\rho_p$ ) thermoelements times their respective area ( $A$ )-to-length ( $\ell$ ) values:

$$R_{\text{int}} = \sum_0^i \left( \rho_n \frac{\ell}{A} + \rho_p \frac{\ell}{A} \right)_i. \quad (66)$$

$P_{\text{max}}$  can be expressed in terms of Seebeck coefficients:

$$P_{\text{max}} = \frac{\left( \sum_0^i (\alpha_n + \alpha_p)_i \right)^2 \Delta T^2}{4R_{\text{int}}}. \quad (67)$$

This expression highlights first important point:  $P_{\text{max}}$  increases with  $\Delta T^2$ . So, for large electrical power output, the largest possible  $\Delta T$  is desired.

The efficiency,  $\Phi$ , with which TEG can convert heat flow,  $Q$ , to electrical power is also important because the most electrical power possible from a given amount of heat flow is desirable. A new expression for the efficiency of a TEG can be obtained starting with expression for  $P_{\text{max}}$ .

The ratio of electrical energy generated per given amount of input heat energy is the definition of efficiency:

$$\Phi = \frac{P_{\max}}{Q}. \quad (68)$$

Eq. (68) can be rewritten, assuming for simplicity a unicouple ( $i = 1$ ), as:

$$\Phi = \frac{(\alpha_n + \alpha_p)^2 \Delta T^2}{4R_{\text{int}}Q}. \quad (69)$$

The flow of heat is dominated by thermal conductivity of the materials from which TEG is constructed, so Fourier's law can be used to express  $Q$ :

$$\Phi = \frac{(\alpha_n + \alpha_p)^2 \Delta T^2}{4R_{\text{int}}([\kappa_n + \kappa_p] \frac{A}{\ell} \Delta T)}. \quad (70)$$

Then expressing  $R_{\text{int}}$  as described earlier:

$$\Phi = \frac{(\alpha_n + \alpha_p)^2 \Delta T^2}{4\left(\rho_n \frac{\ell}{A} + \rho_p \frac{\ell}{A}\right)([\kappa_n + \kappa_p] \frac{A}{\ell} \Delta T)}. \quad (71)$$

For planar TEG devices, the values of  $\ell$  of both n-type and p-type thermoelements are equal; however, cross-sectional areas of n-type and p-type may be quite different. Identifying cross-sectional area of n-type as  $A_n$  and that of p-type as  $A_p$  allows a simplification, yielding  $\Phi$  in terms of measurable materials properties and temperature difference:

$$\Phi = \frac{1}{4} \left( \frac{(\alpha_n + \alpha_p)^2}{\left(\frac{\rho_n}{A_n} + \frac{\rho_p}{A_p}\right)(\kappa_n A_n + \kappa_p A_p)} \right) \Delta T. \quad (72)$$

The proportionality between  $\Phi$  and  $\Delta T$  will be termed “ $Z_{\text{device}}$ ”:

$$Z_{\text{device}} = \left( \frac{(\alpha_n + \alpha_p)^2}{\left(\frac{\rho_n}{A_n} + \frac{\rho_p}{A_p}\right)(\kappa_n A_n + \kappa_p A_p)} \right). \quad (73)$$

Note, that when area-to-length ratios are optimized for maximum efficiency, this relationship reduces to the common, well-known expression for device  $ZT$ :

$$Z_{\max} = \left( \frac{(\alpha_n + \alpha_p)}{(\sqrt{\kappa_n \rho_p} + \sqrt{\kappa_p \rho_n})} \right)^2. \quad (74)$$

TEG efficiency can be measured as function of  $\Delta T$ , and the slope of that data should be equal to:

$$\frac{\partial \Phi}{\partial \Delta T} = \frac{1}{4} \left( \frac{(\alpha_n + \alpha_p)^2}{\left(\frac{\rho_n}{A_n} + \frac{\rho_p}{A_p}\right)(\kappa_n A_n + \kappa_p A_p)} \right) = \frac{Z_{\text{device}}}{4}. \quad (75)$$

This expression highlights a second important point, that  $\Phi$  should linearly increase as a function of  $\Delta T$  according to the slope indicated by  $1/4$  of the quantity in parentheses. This makes sense, because  $\Phi$  increases linearly with  $\Delta T$ , and  $P_{\text{max}}$  increases as  $\Delta T^2$ . Taking the ratio yields a simple linear dependence on  $\Delta T$ . Note, that the material properties are all temperature dependent, so taking the derivative would necessarily yield higher-order terms. However, we make use of the following assumptions: (1) the temperature dependence of the electrical component of thermal conductivity depends on the mobility of charge carriers, and the electrical resistivity depends on the inverse of that mobility, so these dependencies can be assumed to be first-order to cancel completely. (2) Seebeck coefficient does have a relatively small, but finite temperature dependence; however the derivative of Seebeck coefficient should yield a temperature dependence of  $T^{-1}$  which approximately cancels with the temperature dependence of lattice thermal conductivity in the denominator. So, to first order the linearity of the slope would be expected, and is in fact experimentally observed as will be shown.

A new index to determine maximum ZT of TEG device can be obtained by measuring the slope of TEG efficiency. To calculate maximum ZT, four times the slope of TEG efficiency multiplied by maximum temperature, under which TEG displays linear behavior with respect to  $\Delta T$ . Outside the linear regime of TEGs, the basic properties can no longer be described by these functions. Therefore, measure of maximum ZT of TEG device can be determined by:

$$(\text{Maximum})Z_{\text{device}}T = 4 \left( \frac{(\alpha_n + \alpha_p)^2}{\left(\frac{\rho_n}{A_n} + \frac{\rho_p}{A_p}\right)(\kappa_n A_n + \kappa_p A_p)} \right) T_{\text{maximum}}. \quad (76)$$

The significance of this analysis is that it allows unique means to rapidly obtain  $ZT_{\text{maximum}}$  and confirm properties and individual measurements. Measurements can be confirmed by measuring slope of efficiency as function of  $\Delta T$  and ZT can be obtained and compared to theoretical ZT as calculated by individual measurements.

### 3.1.1. Analysis of commercial $(\text{Bi,Sb})_2(\text{Te,Se})_3$ module

Efficiency of commercial  $(\text{Bi,Sb})_2(\text{Te,Se})_3$  device is presented in **Figure 18**. This device is designed for high thermal impedance and has optimum performance window from nearly room-temperature to roughly 425 K. Slope of efficiency was determined and is shown in inset of **Figure 18**, and is given as 0.0004/K. As expected, the slope is highly linear function of  $\Delta T$  until deviation from non-linearity begins at 405 K. The maximum ZT can be obtained by the simple relationship, and observed maximum temperature of roughly 405 K:

$$Z_{\text{device}}T_{\text{maximum}} = 4 \left( \frac{\partial \Phi}{\partial \Delta T} \right) T_{\text{maximum}}. \quad (77)$$

Obtained value of  $ZT_{\text{maximum}}$  is equal to 0.7, which is consistent with established values for commercial devices.

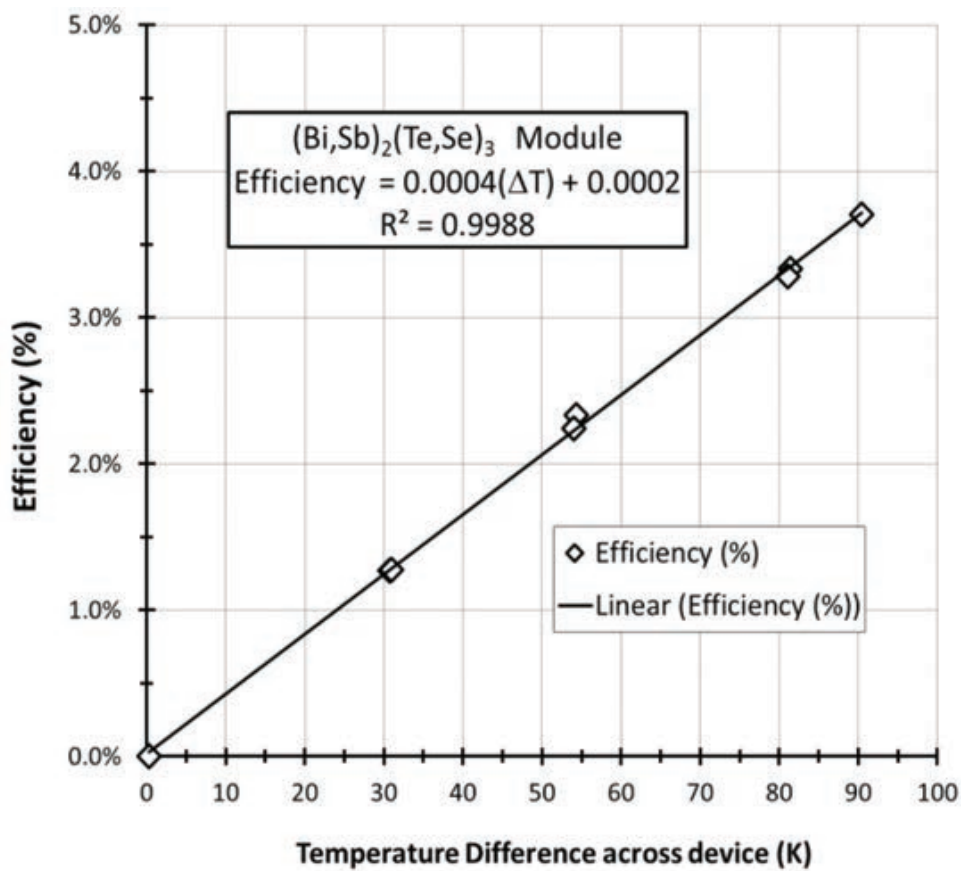


Figure 18. Slope of efficiency from  $(\text{Bi,Sb})_2(\text{Te,Se})_3$  to determine  $ZT_{\text{max}}$ .

### 3.1.2. Analysis of PbTe/TAGS module

Efficiency of PbTe/TAGS device is presented below. Figure 19 shows temperature dependence of PbTe/TAGS module efficiency. At low temperature, the slope is somewhat a nonlinear function of  $\Delta T$  because, it is well known, that properties of these materials are uninteresting at low-temperature, but optimum at elevated temperature. So, slope of efficiency is measured in temperature range  $>500$  K, where properties are linear. The maximum  $ZT$  can, therefore, be obtained by Eq. (77), and observed maximum temperature for linear device behavior, which for the device being measured is equal to 873 K. Obtained slope is 0.0002/K resulting in value  $ZT_{\text{maximum}} = 0.7$ , which is consistent with established values for well-known PbTe/TAGS modules.

## 3.2. Discretized heat-balance model and analysis

More detailed device analysis and performance modeling including effects of temperature-dependent material properties may be accomplished through the use of numerical methods. One technique for performing numerical analysis on TEG was reported by Lau and Buist [26] and later confirmed and expanded upon by Hogan and Shih [27]. It involves partitioning the legs of TEG into virtual segments for computational purposes, where each segment is taken to be isothermal. Neighboring segments then vary in temperature such, that governing thermoelectric heat balance equations based on constant parameter theory are satisfied [28, 29]. This process is illustrated in Figure 20.

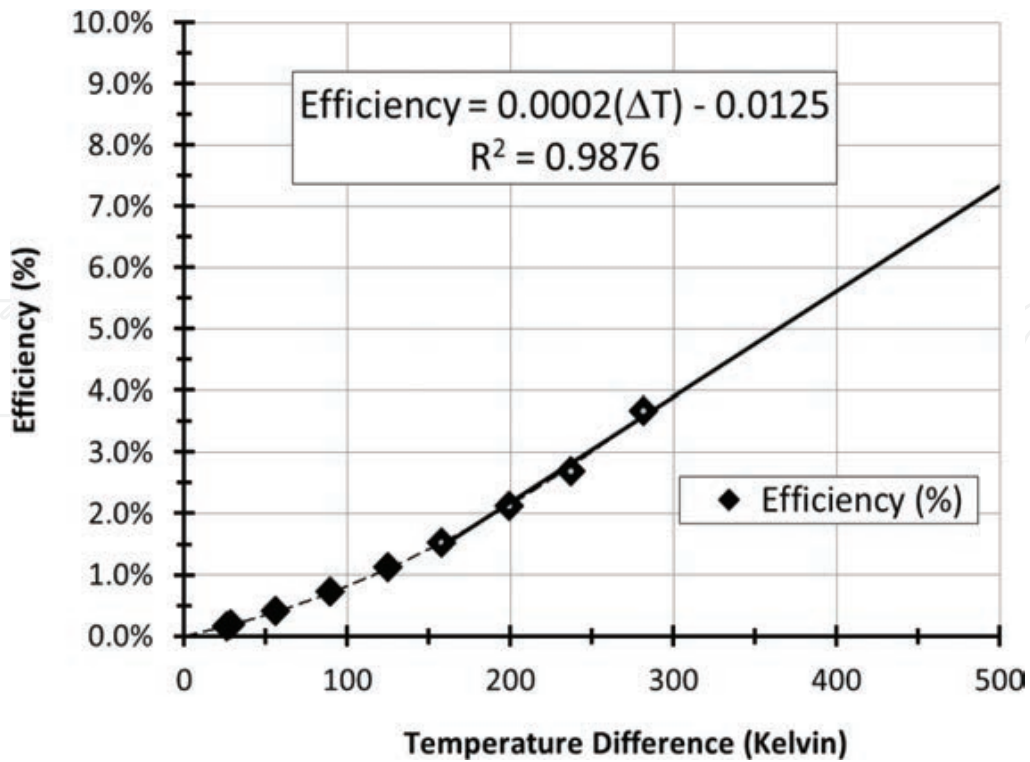


Figure 19. Slope of efficiency from pre-commercial PbTe/TAGS to determine  $ZT_{max}$ .

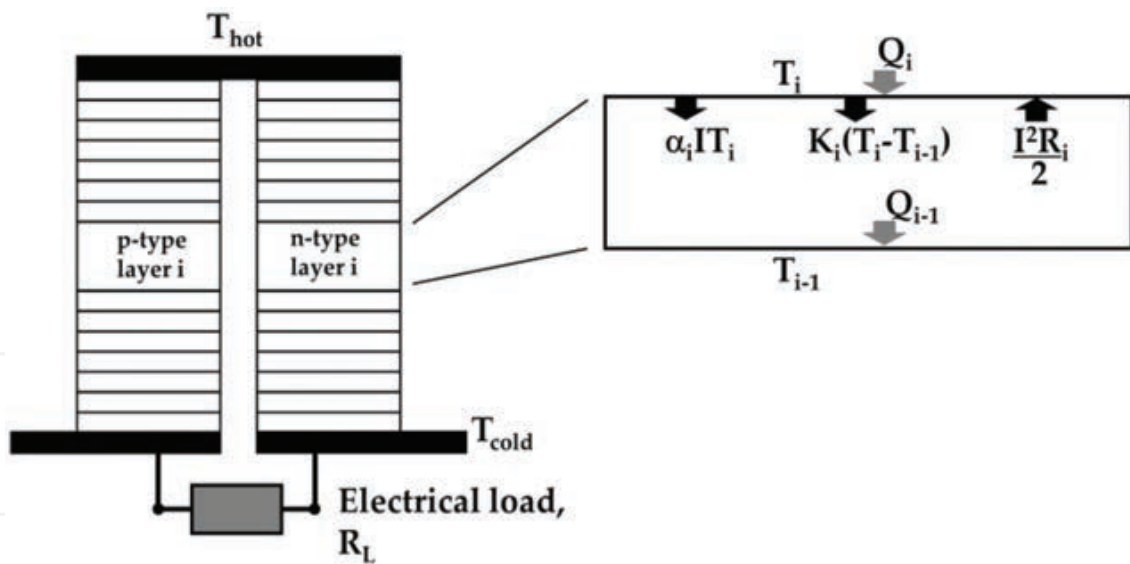


Figure 20. Discrete communicating layers having thermal and electrical flux continuity. Expanded view of  $i^{th}$  segment explicitly showing the heat flows that must be balanced to maintain continuity through the bulk of the TEG device.

Based on constant-parameter theory [29] and heat balance at the top surface of the  $i^{th}$  segment, we have:

$$Q_i = a_i I T_i - I^2 R_i / 2 + K_i (T_i - T_{i-1}), \tag{78}$$

where the total heat flux  $Q_i$  into segment is the sum of individual components indicated.

Here  $\alpha_i$  is Seebeck coefficient of the  $i^{\text{th}}$  segment at temperature  $T$ ,  $R_i$  is the electrical resistance of the  $i^{\text{th}}$  segment at temperature  $T$ ,  $K_i$  is thermal conductance of the  $i^{\text{th}}$  segment at temperature  $T$ . Last,  $I$ , and  $T_i$  are the electrical current and temperature of the  $i^{\text{th}}$  segment, respectively. The electrical power,  $P$ , is determined by:

$$Q_{i-1} = Q_i - P, \quad (79)$$

where power  $P$  is delivered to the external load resistor,  $R_L$ :

$$P = I^2 R_L. \quad (80)$$

The discrete heat balance equations (Eqs. (78) and (79)) derived in this manner can be easily solved for single leg of TEG with an iterative technique [26, 27]. For a given  $T_C$ , an initial estimate is made for the heat delivered to the cold junction,  $Q_C$ , and temperature and heat flow in each segment is determined sequentially, ending with a numerical solution for heat absorbed at the hot junction  $Q_H$  and the hot-side temperature  $T_H$ . If calculated  $T_H$  is not equal to the desired  $T_H$  boundary condition, then  $Q_C$  is adjusted accordingly and the process is repeated until the desired  $T_H$  is achieved.

The initial hot-side temperature of segment is taken as a uniform temperature for the entire segment and its thermoelectric properties are then determined from a curve fit to measured data. Adjacent segments attain different temperatures as the system is solved according to the energy balance requirements. Thus, temperature-dependent effects are fully incorporated into the model. In fact, Hogan and Shih [27] were able to demonstrate excellent agreement using the discrete approximation as compared with an exact analysis of temperature-dependent TEG performance by Sherman et.al. [30].

**Figure 21** shows temperature profiles calculated for n-type Skutterudite material with temperature-dependent properties, operating at the indicated boundary conditions. For simplicity, electrical current is treated here as though there were an external load resistance matched to the internal resistance of the thermoelectric material leg, thus producing maximum output power.

It is also instructive to examine calculated heat flow through the leg as this helps to illustrate thermal-to-electrical conversion process. **Figure 22** shows heat flow corresponding to temperature profiles depicted in **Figure 21**. From the hot side to the cold side of the leg (or right to left on the plot), heat flow is reduced as thermal energy is converted to electrical power and delivered to the load. Examining the specific case of  $T_H = 750$  K and  $T_C = 300$  K, there is approximately 5.7 W of thermal power incident on the hot side and 5.0 W rejected at the cold side, leaving 0.7 W which is delivered as electrical power to the load. So the conversion efficiency within just one of the legs of the TEG itself is simply  $0.7 \text{ W}/5.7 \text{ W} = 12.3\%$ . The same methodology may be applied to the companion p-type leg to complete the analysis of a full TEG at a given set of temperature boundary conditions. Proper temperature profiles of n-type and p-type legs together are shown in **Figure 23**. Taking  $T_H = 800$  K and  $T_C = 300$  K, the combined incident thermal power is equal to  $6.42 \text{ Watts}_{\text{thermal}}$  (n-type) +  $7.85 \text{ Watts}_{\text{thermal}}$  (p-type) =  $14.27 \text{ Watts}_{\text{thermal}}$  (TEG). And that rejected to the cold side is equal to  $5.58 \text{ Watts}_{\text{thermal}}$  (n-type) +  $7.16 \text{ Watts}_{\text{thermal}}$  (p-type) =  $12.74 \text{ Watts}_{\text{thermal}}$  (TEG). This calculation finds the overall efficiency =  $1.53 \text{ W}/14.27 \text{ W} = 10.7\%$ .

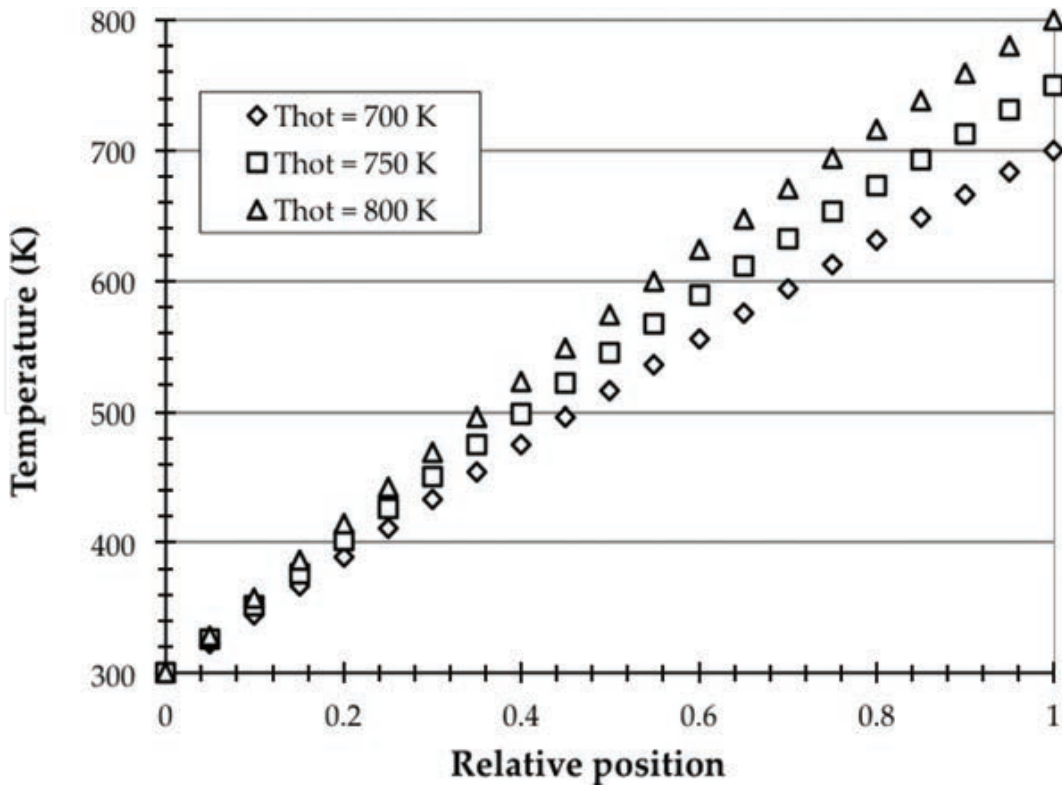


Figure 21. Temperature profile in n-type Skutterudite at maximum power.  $T_C = 300$  K.

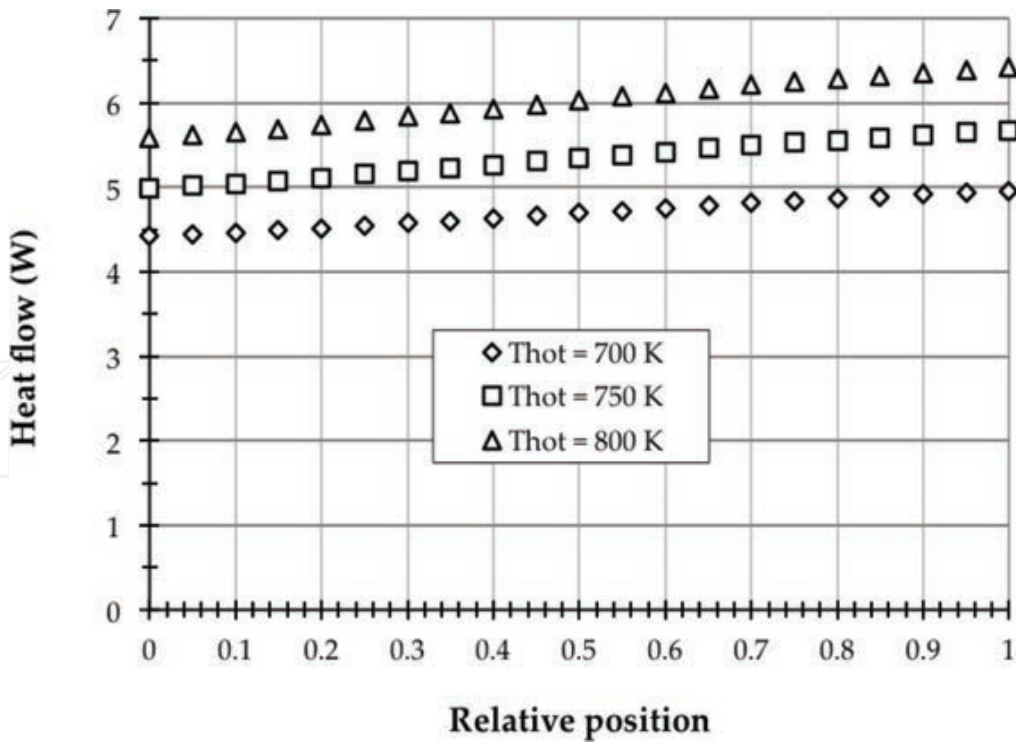


Figure 22. Heat flow profile in n-type Skutterudite sample at maximum output power, corresponding to temperature profiles depicted in Figure 21.  $T_C = 300$  K.

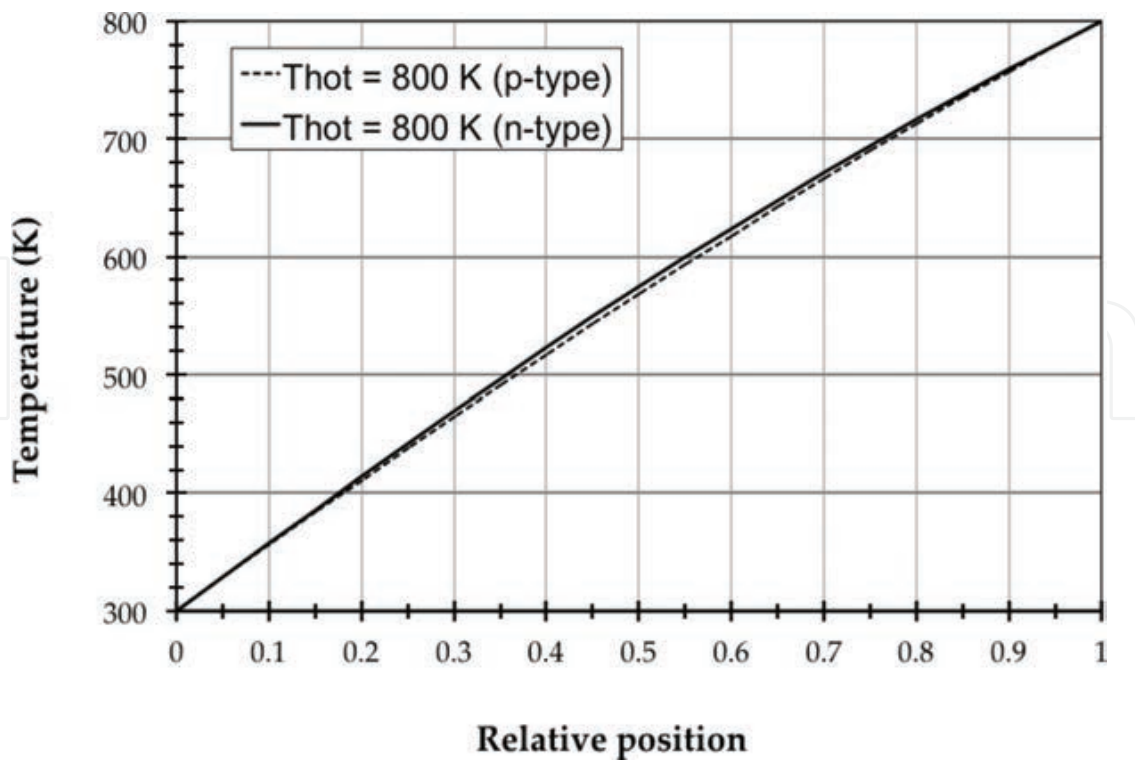


Figure 23. Temperature profiles in both n- and p-type legs of TEG.  $T_C = 300$  K.

This discussion has highlighted a simple, but powerful temperature-dependent phenomenological model for precisely calculating temperature profiles, heat flows, power outputs, and efficiencies in a single leg of TEG. Full TEG device modeling is accomplished by simultaneously solving the discrete heat balances as described for each leg (subject to hot side and cold side boundary conditions) along with the simultaneous energy balance relationship required for electrical power being delivered to the load.

Figure 24 shows calculated efficiency using the *discretized heat balance* theory of idealized Skutterudite n-type and Skutterudite p-type devices.

Electrical and thermal contact resistivities are defined to be zero, but could easily be included as finite quantities, which would add penalties to the efficiency. Slope of efficiency identified in the best-fit is quantified first using unitless efficiency data. The equation is then re-included on the plot after converting to percent. This is so that  $ZT_{\text{maximum}}$  can be calculated using **slope/efficiency method** described in Section 3.1, and for overall clarity in the final plot. Slope of efficiency is 0.0002/K, and the upper-limit temperature is 800 K, so, following Eq. (77), value  $ZT_{\text{maximum}} = 0.64$  is obtained for the device.

Therefore, to confirm measurements for device fabricated using materials, from which measurements were collected, it could be assembled and the efficiency is measured. If measurements are accurate and not overestimated, then performance should be consistent with  $ZT_{\text{maximum}}$  value equals to 0.64. The slope of the data should be roughly 0.0002/K.

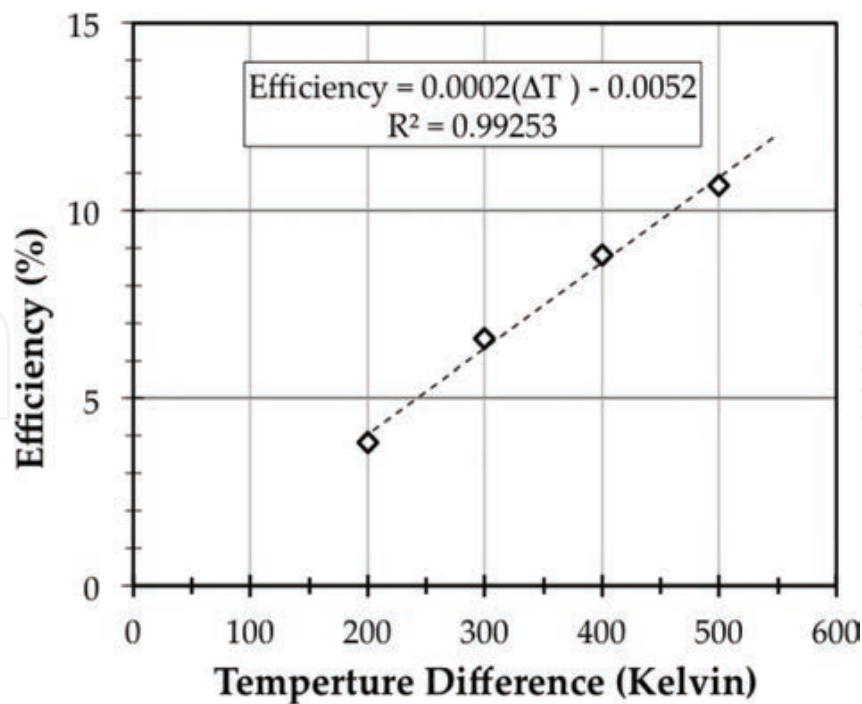


Figure 24. Calculated efficiency of single p-n couple TEG.  $T_C = 300$  K and  $T_{h(max)} = 800$  K.

## 4. Conclusions

In conclusion, we have presented several novel approaches to the significant challenge of accurately determining the thermal conductivity of thermoelectric materials. The new solutions can be much faster experimentally, and they successfully address several sources of experimental error. The overall result is significantly reduced error, which may reduce uncertainty by a factor of 2 or more. Further, we introduce new approaches to compare device performance with physical property measurements as a novel means of confirming measurements. Using this approach, the new measurements can be clearly seen to yield physical property measurements which are more consistent with physical device performance.

The first new thermal conductivity measurement method, *steady-state isothermal technique*, improves accuracy by collecting data under conditions where thermal losses and errors are unimportant. The validity was confirmed by comparing the thermal conductivity extracted from a Peltier cooling device with the lab measured value: the error was  $\sim 2\%$  [8]. The second is nondestructive micro-scale analysis technique called the *scanning hot-probe*, and the third is *lock-in transient Harman* method, which is a comprehensive modification of transient Harman technique. The second and third methods reduce error by highly detailed treatment of interfacial contact effects including electrical contact resistance and thermal contact effects. The high accuracy for both of these methods is obtained by comparison with established standard reference materials whose properties are well-known and accepted. A new interesting follow-on is frequency-dependent Nyquist analysis, which presages a different perspective on the materials analysis, and even further simplified measurement.

The truest test of the accuracy of measurement is comparison with fabricated devices. To support the validation of measurements of individual material properties, we have outlined new device metrics, which allows comparison between theoretical and measured device efficiency. We outline a new *slope-efficiency method*, which can be used to determine informative index  $ZT_{\text{maximum}}$  of any device. The second method of device evaluation is a numerical device model called the *discretized heat balance model*. Using this modeling approach, we showed, that a piecewise continuous collection of discrete layers within a device, where boundary heat flows have energy and current continuity relationships, can yield an incredibly easy theoretical determination of device efficiency, which can be compared with experimental values.

## Author details

Patrick J. Taylor<sup>1\*</sup>, Adam Wilson<sup>1,2</sup>, Jay R. Maddux<sup>1,3</sup>, Theodorian Borca-Tasciuc<sup>2</sup>, Samuel P. Moran<sup>2</sup>, Eduardo Castillo<sup>2</sup> and Diana Borca-Tasciuc<sup>2</sup>

\*Address all correspondence to: [patrick.j.taylor36.civ@mail.mil](mailto:patrick.j.taylor36.civ@mail.mil)

1 US Army Research Laboratory, Sensors and Electron Devices Directorate, Adelphi, MD, USA

2 Department of Mechanical, Aerospace and Nuclear Engineering, Rensselaer Polytechnic Institute, Troy, NY, USA

3 General Technical Services, NJ, USA

## References

- [1] Wang H, Bai S, Böttner S, Chen L, Harris F, Kiss L, Kleinke H, König J, Lo J, Mayolet A, Porter W, Sharp J, Smith C, Tritt T. Transport properties of bulk thermoelectrics-an international round-robin study, Part I: Seebeck coefficient and electrical resistivity. *Journal of Electric Materials*. 2013;**42**:4 p.654–664. DOI: 10.1007/s11664-012-2396-8
- [2] Putley E. Thermoelectric and galvanomagnetic effects in lead selenide and telluride. *Proceedings of the Physical Society. Section B*. 1955;**68** p.35. DOI: 10.1088/0370-1301/68/1/306
- [3] Harman T, Cahn J, Logan M. Measurement of thermal conductivity by utilization of the Peltier effect. *Journal of Applied Physics*. 1959;**30**:9 p.1351. DOI: 10.1063/1.1735334
- [4] Penn A. The correction used in the adiabatic measurement of thermal conductivity using the Peltier effect. *Journal of Scientific Instruments*. 1964;**41**:10 p.626. DOI: 10.1088/0950-7671/41/10/311

- [5] Bowley A, Cowles L, Williams G, Goldsmid H. Measurement of the figure of merit of a thermoelectric material. *Journal of Scientific Instruments*. 1961;**38**:11 p.433. DOI: 10.1088/0950-7671/38/11/309
- [6] Buist R. A new method for testing thermoelectric materials and devices. In: Proceedings of the 11th International Conference on Thermoelectrics (ICT '92); 7–9 October 1992; Arlington, Texas. Available from: <https://www.titech.com/wp-content/uploads/2013/10/ICT92RJB.tif> [accessed 2016-08-22]
- [7] Taylor P, Jesser W, Rosi F, Derzko Z. A model for the non-steady-state temperature behaviour of thermoelectric cooling semiconductor devices. *Semiconductor Science and Technology*. 1997;**12**:4 p.443. DOI: 10.1088/0268-1242/12/4/018
- [8] Taylor P, Maddux J, Uppal P. Measurement of thermal conductivity using steady-state isothermal conditions and validation by comparison with thermoelectric device performance. *Journal of Electronic Materials*. 2012;**41**:9 p.2307. DOI: 10.1007/s11664-012-2178-3
- [9] Joshi G, Yan X, Wang H, Liu W, Chen G, Ren. Enhancement in thermoelectric figure-of-merit of an N-type half-Heusler compound by the nanocomposite approach. *Advanced Energy Materials*. 2011;**1**:4 p.643. DOI: 10.1002/aenm.201100126
- [10] Rosi F, Hockings E, Lindenblad N. Semiconducting materials for thermoelectric power generation. *RCA (Radio Corporation of America) Review*. 1961;**22**. OSTI: 4838510
- [11] Wilson A, Munoz M, Abad B, Perez J, Maiz J, Schomacker J, Martin-Gonzalez M, Borca-Tasciuc D, Borca-Tasciuc T. Thermal conductivity measurements of high and low thermal conductivity films using a scanning hot probe method in the  $3\omega$  mode and novel calibration strategies. *Nanoscale*. 2015;**7**: p.15404–15412. DOI: 10.1039/C5NR03274A
- [12] Borca-Tasciuc T. Scanning probe methods for thermal and thermoelectric property measurements. *Annual Review of Heat Transfer*. 2013;**16**:80 p.211–258. DOI: 10.1615/AnnualRevHeatTransfer.v16.80
- [13] Lefèvre S, Volz S, Chapuis P. Nanoscale heat transfer at contact between a hot tip and a substrate. *International Journal of Heat and Mass Transfer*. 2006;**49**:1–2 p.251. DOI: 10.1016/j.ijheatmasstransfer.2005.07.010
- [14] Incropera F, DeWitt D. *Fundamentals of heat and mass transfer*. 5th ed. New York: Wiley; 2002. ISBN: 0471386502
- [15] Son Y, Pal S, Borca-Tasciuc T, Ajayan P, Siegel R. Thermal resistance of the native interface between vertically aligned multiwalled carbon nanotube arrays and their SiO<sub>2</sub>/Si substrate. *Journal of Applied Physics*. 2008;**103**:2 p.024911. DOI: 10.1063/1.2832405
- [16] Taborda J., Romero J, Abad B, Muñoz-Rojo M, Mello A, Briones F, and Gonzalez M. Low thermal conductivity and improved thermoelectric performance of nanocrystalline silicon germanium films by sputtering. *Nanotechnology*. 2016;**27**:17. p.175401. DOI: 10.1088/0957-4484/27/17/175401

- [17] Maiz J, Rojo M, Abad B, Wilson A, Nogales A, Borca-Tasciuc D, Borca-Tasciuc T, Martín-González M. Enhancement of thermoelectric efficiency of doped PCDTBT polymer films. *RSC Advances*. 2015;**82**:5 p.66687–66694. DOI: 10.1039/C5RA13452H
- [18] Abad B, Rull-Bravo M, Hodson S, Xu X, Martín-González M. Thermoelectric properties of electrodeposited tellurium films and the sodium lignosulfonate effect. *Electrochimica Acta*. 2015;**169**: p.37. DOI: 10.1016/j.electacta.2015.04.063
- [19] Langer G, Hartmann J, Reichling M. Thermal conductivity of thin metallic films measured by photothermal profile analysis. *Review of Scientific Instruments*. 1997;**68**: p.1510. DOI: 10.1063/1.1147638
- [20] Abad B, Alda I, Díaz-Chao P, Kawakami H, Almarza A, Amantia D, Gutierrez D, Aubouy L, Martín-González M. Improved power factor of polyaniline nanocomposites with exfoliated graphene nanoplatelets (GNPs). *Journal of Materials Chemistry A*. 2013;**1**:35 p.10450. DOI: 10.1039/C3TA12105D
- [21] Castillo E, Hapenciuc C, Borca-Tasciuc T. Thermoelectric characterization by transient Harman method under non-ideal contact and boundary conditions. *Review of Scientific Instruments*. 2010;**81**:4 p.044902. DOI: 10.1063/1.3374120
- [22] Ivory J. Rapid method for measuring Seebeck coefficient as  $\Delta T$  approaches zero. *Review of Scientific Instruments*. 1962;**33**:9 p.992. DOI:10.1063/1.1718048
- [23] Sharp J, Bierschenk J, Lyon Jr. H. Overview of solid-state thermoelectric refrigerators and possible applications to on-chip thermal management. *Proceedings of the IEEE*. 2006;**94**:8 p.1602. DOI: 10.1109/JPROC.2006.879795
- [24] De Marchi A, Giaretto V. An accurate new method to measure the dimensionless figure of merit of thermoelectric devices based on the complex impedance porcupine diagram. *Review of Scientific Instruments*. 2011;**82**:10 p.104904. DOI: 10.1063/1.3656074
- [25] Efremov M, Olson E, Zhang M, Lai S, Schiettekatte F, Zhang Z, Allen L. Thin-film differential scanning nanocalorimetry: Heat capacity analysis. *Thermochimica Acta*. 2004;**412**:1 p.13. DOI: 10.1016/j.tca.2003.08.019
- [26] Lau P, Buist R. Calculation of thermoelectric power generation performance using finite element analysis. In: *Proceedings of the 16th International Conference on Thermoelectrics (ICT '97)*; 26–29 August 1997; Dresden, Germany. New York: IEEE; 1997. p.563.
- [27] Hogan T, Shih T. Modeling and Characterization of Power Generation Modules Based on Bulk Materials. In: Rowe D, editor. *Thermoelectrics Handbook: Macro to Nano*. 1st ed. Washington DC: CRC Press; 2005. p.12–21. DOI: 10.1201/9781420038903.ch12
- [28] Buist R. Calculation of Peltier Device Performance. In: Rowe D, editor. *CRC Handbook of Thermoelectrics*. 1st ed. Washington DC: CRC Press; 1995. p.143–156. DOI: 10.1201/9781420049718.ch14

- [29] Cobble M. Calculation of Generator Performance. In: Rowe D, editor. CRC Handbook of Thermoelectrics. 1st ed. Washington DC: CRC Press; 1995. p.489. DOI: 10.1201/9781420049718.ch39
- [30] Sherman B, Heikes R, Ure R. Calculation of efficiency of thermoelectric devices. Journal of Applied Physics. 1960:31: p.1. DOI: 10.1063/1.1735380

IntechOpen

IntechOpen